

Production of Antibacterial Activity and Bone Cell Proliferation by Surface Engineering of Ga- or Mn-Doped Ceria-Coated Biomedical Titanium Alloy

Ayda Khosravanihaghighi,* Pramod Koshy, Muhammad Yasir, Sara Romanazzo, Vedran Lovric, Kristopher Alan Kilian, Mark Duncan Willcox, William Robert Walsh, and Charles Christopher Sorrell

The present work reports a detailed interpretation of the role of Ga and Mn dopants, solid solubility mechanisms, charge compensation mechanisms, intervalence charge transfer, antibacterial performance, and cell attachment and proliferation. Sol-gel undoped and doped (1, 5, and 9 mol%) CeO₂ films are spin-coated on 3D printed Ti6Al4V biomedical alloy substrates and annealed at 650 °C for 2 h in air. Material characterization includes scanning electron microscopy (SEM), 3D scanning laser confocal microscopy, glancing angle X-ray diffraction (GAXRD), and X-ray photoelectron spectroscopy (XPS). In vitro testing includes inhibition of bacterial growth, simulated body fluid (SBF) testing, and cell attachment and proliferation studies. The most significant outcome is that the bioactivity of ceria derives directly from the Ce³⁺ concentration, which itself results from solid solubility (substitutional and interstitial) and charge compensation and redox. This challenges the common assumption of the dominance of oxygen vacancies in the performance of ceria. The antibacterial activity is dependent on the type, amount, and valence of the dopant, where opposite trends are observed for gram-positive *Staphylococcus aureus* and gram-negative *Escherichia coli* bacteria. All of the doped samples result in enhanced cell proliferation, although this is greatest at the lowest dopant concentration. Surface hydroxyapatite formation on the samples is achieved by soaking in SBF at 2 weeks and 1 month.

some implants will require revision arthroplasty. Hence, a 2017 survey by the National Joint Registries (NJR) of Australia^[2] revealed that primary arthroplasty surgeries in Australia increased by 5.7% and 1.1% for knee and hip replacements, respectively, while the respective revision surgeries increased by 7.4% and 8.9%. These numbers were slightly different in a similar survey for the US,^[3] where primary arthroplasty surgeries for knee and hip replacements increased, respectively, 8.2% and 27.3% and revision by 9.1% and 5.6%.

Of the two leading causes of implant failures, bacterial infection accounted for ≈20% of failures and poor osseointegration was responsible for ≈18% of failures.^[4] In many cases, bacterial infection remains the principal cause of implant failure.^[5–7] Two of the most common bacteria found at infected implant sites are *Staphylococcus aureus* and *Escherichia coli*, which are gram-positive and gram-negative, respectively.^[8,9] *S. aureus* is responsible for approximately two-thirds of all implant infections.^[10,11]

If bacteria attach and propagate on implants, the resultant infection can lead to implant failure. In addition, the success of an implant after surgery is strongly dependent on the adhesion and growth of healthy cells, which results in osseointegration followed by tissue integration.^[12] Osseointegration depends on success in fixation initially, during

1. Introduction


It has been predicted that the demand for arthroplasty surgeries in the US by 2030 will increase by 673% and 174% for knee and hip replacement surgeries, respectively.^[1] It is inevitable that

A. Khosravanihaghighi, P. Koshy, K. A. Kilian, C. C. Sorrell
School of Materials Science and Engineering
UNSW
Sydney, NSW 2052, Australia
E-mail: ayda.khosravani@gmail.com

M. Yasir, M. D. Willcox
School of Optometry and Vision Science
UNSW
Sydney, NSW 2052, Australia

S. Romanazzo, K. A. Kilian
School of Chemistry
UNSW
Sydney, NSW 2052, Australia

V. Lovric, W. R. Walsh
Prince of Wales Clinical School
UNSW
Sydney, NSW 2052, Australia

 The ORCID identification number(s) for the author(s) of this article can be found under <https://doi.org/10.1002/adem.202200077>.

DOI: 10.1002/adem.202200077

surgery, and postoperatively. However, aseptic loosening can occur owing to implant micromotion relative to the host bone, which triggers the generation of wear particles and consequent inflammation.^[4] Although aseptic loosening and bacterial infection generally are unrelated, recent work has revealed that aseptic loosening can stimulate bacterial infection.^[13] Consequently, it is relevant to examine both issues simultaneously despite their general acceptance as independent variables.

Orthopedic materials include a range of polymers, ceramics, and metals.^[14] Metallic materials are favored for many load-bearing applications largely owing to their suitable chemical durability, high tensile strength, limited elasticity, and adequate wear resistance. The most favorable choice of such materials depends on a combination of design, structural, microstructural, mechanical, chemical, and physiological issues.^[15]

Titanium-based alloys have emerged as the lead metallic material for implants owing to their bioinertness, biocompatibility, and potential for the introduction of bioactivity through surface modification. Pure titanium is used mostly for dental implants, whereas the biomedical titanium alloy Ti6Al4V is used most commonly for orthopedic implants. The presence of aluminum and vanadium enhances the mechanical strength of the alloy.^[16] Materials applied to the surface to enhance bioactivity include in situ passivating TiO₂,^[17] ex situ applied TiO₂,^[18] hydroxyapatite (HA),^[19] hybrid inorganic–organic coating,^[20] glass-ceramic coating,^[21] and ceramic-metal composite coating.^[22]

One of the key approaches to prevent the adhesion and colonization of bacteria on implants is to modify their surface,^[23] thus allowing bone cells to attach to the surface.^[4] Antibacterial approaches include antiadhesive coatings,^[24] bactericidal coatings,^[25] and altered surface topographies (to expose nanowires,^[26] nanotubes,^[27] or cicada wings-like biomimetic surface^[28]). The cell-attachment approaches include calcium phosphate coatings,^[29] biomolecular coatings,^[30] and engineered surface topographies.^[31] CeO₂ or ceria has emerged as a key biocatalytic material.^[32,33] However, its applicability as a surface coating has not been explored extensively even though ceria has been shown to have antimicrobial activity. The key materials variables that can be engineered to improve the performance are summarized in Table S1, Supporting Information.

Contact between ceria and bacteria can result in destruction of the bacteria by several mechanisms, including cell wall disruption; oxidative stress from the generation of reactive oxygen species; chemical degradation of bacterial DNA, RNA, and proteins; as well as dysregulation of nutrient transport.^[34,35] Ceria also can interfere with bacterial respiration and electron flow,^[36] followed by reaction with thiol (–SH) groups or adsorption on transporters and resultant hindrance of nutrient transportation.^[37,38]

The two main strategies for promoting osseointegration of implant materials are alteration of the implant surface topography and deposition of a coating to enhance implant biocompatibility, cell adhesion, cell proliferation, and hence bone regeneration.^[39] Alteration of implant surface topography changes the surface microstructure or nanostructure to improve interactions between bone cells and implant surface,^[4] generally by roughening the surface topography for mechanical interlocking.^[40] Surface coatings on metallic implants to improve bone tissue deposition and in-growth at the implant surface include calcium phosphate coatings,^[41] bioactive glass

coatings,^[42] bioinert oxide coatings,^[43] and biomolecular coatings.^[44]

There also are strategies to combine the hindrance of bacterial infection and the enhancement of osseointegration. These include the insertion of therapeutic ions^[45–51] into resorbable metallic alloys,^[52] resorbable bioceramics,^[53] and resorbable biomolecules^[54] as well as doping of the surfaces by methods such as diffusion^[55] and ion implantation.^[56] Relevant information about these therapeutic ions is summarized in Table S2, Supporting Information.

In addition to ceria's direct antimicrobial action, it can be doped with other substances to enhance this activity. Ga³⁺ has been shown to exhibit bactericidal activity upon substitution for biological Fe³⁺, which plays a key role in a microorganism's metabolic processes, including respiration, oxygen transport, DNA regulation, and survival of bacteria.^[57,58] Ga³⁺ has been reported not only to accelerate early osteoblastic differentiation but also to interrupt osteoclastogenesis albeit as an adsorbed salt rather than a solid solute.^[59,60] The bactericidal activity of Mn has been reported to result from the formation of reactive oxygen species (ROS) at the nanoparticle surfaces. Mesaros et al.^[61] reported that interstitial solid solubility of Mn²⁺ in ZnO and the associated electronic charge compensation resulted in enhanced antibacterial activity, presumably through the generation of hydroxyl radicals. Mn²⁺ also has been shown to have promising effects on implant bone in-growth the strong affinity with extracellular matrix proteins.^[62–64]

The aims of the current research were to investigate the effects of the doping of CeO₂ thin films deposited on biomedical grade Ti6Al4V alloy by Ga as proxy for Fe and by Mn in terms of the antibacterial performance and osteoblastic cell proliferation.

2. Results and Discussion

2.1. Sample Nomenclature

There were four types of samples: 1) Uncoated: Ti6Al4V substrate; 2) CeO₂-coated: undoped CeO₂ thin film on substrate; 3) Ga-doped: CeO₂ thin films on substrate; doped with Ga at levels of: a) 1 mol% (1GC), b) 5 mol% (5GC), and c) 9 mol% (9GC); 4) Mn-doped: CeO₂ thin films; doped with Mn at levels of: a) 1 mol% (1MC); b) 5 mol% (5MC); and c) 9 mol% (9MC).

2.2. Material Characterization

Figure 1 shows the nanostructures of the thin films the text read. **Figure 1a** shows a characteristic cross section that reveals that the substrate was uneven, the thin films were porous, the substrate/coating interface was intimate, and the top surface of the thin film was rough. **Figure 1b–e** highlights the protrusion of the asperities of the 3D printed substrate, the filling of the interstices with the sol–gel precursor, and the drying or calcining cracks in the thin films. The top surfaces of the thin films not shown were similar to that of **Figure 1e**.

Further, the artifacts of the asperities suggest the relative viscosities of the sol–gel precursors. That is, the low viscosity of the CeO₂-coated film results in fluid flow into the voids, leaving thinly coated small spheres as asperities. The intermediate

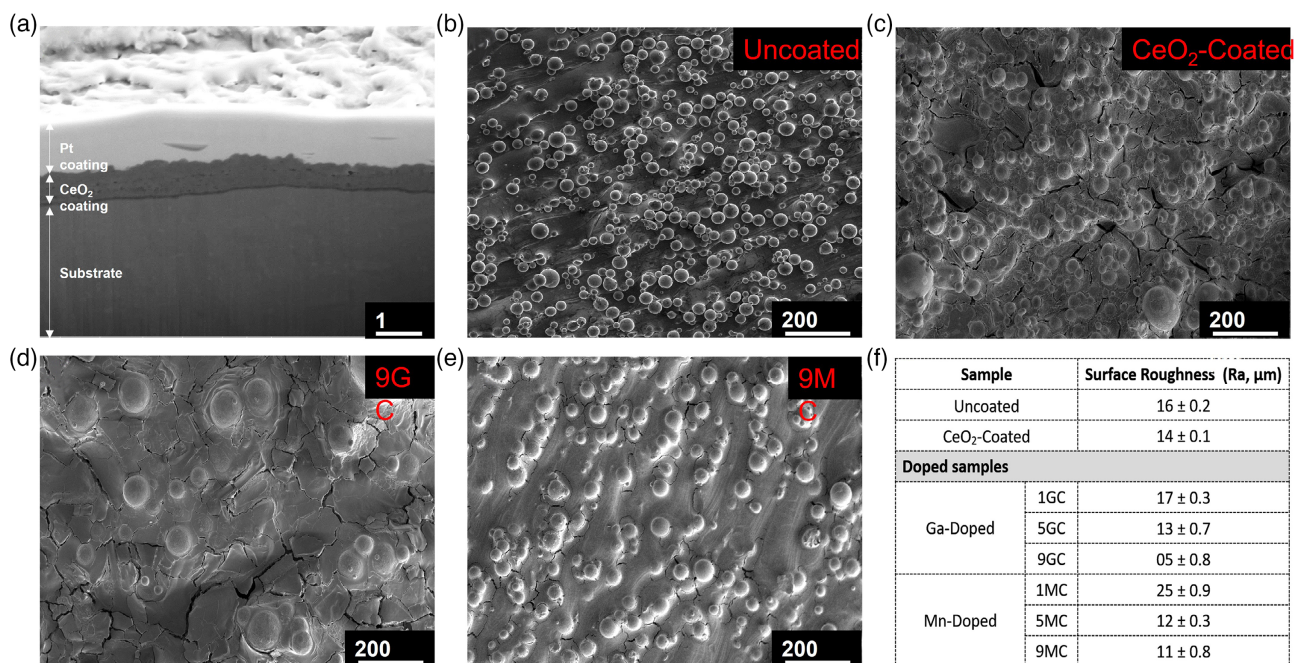


Figure 1. FIB image: a) cross section of undoped CeO₂-coated sample; SEM images: b) uncoated substrate, c) undoped CeO₂ coating, d) 9 mol% Ga-doped CeO₂ coating, e) 9 mol% Mn-doped CeO₂ coating; f) tabulated summary of roughnesses (R_a) determined by 3D laser scanning confocal microscopy; all coatings calcined at 650 °C for 2 h.

viscosity of the 9MC thin film shows increased filling of the voids with little change in the sizes of the spherical asperities. The high viscosity of the 9GC thin film shows a low concentration of thickly coated spheres of large size. This interpretation is confirmed by the tabulated data in Figure 1f, which reveals R_a roughnesses in the order uncoated > CeO₂-coated > 9MC > 9GC. This trend is consistent with the effect of ionic field strength (valence/radius) for the three compositions. This ranking and the field emission scanning electron microscopy (FESEM) images suggest that, with increasing dopant levels, the R_a roughness of the Mn-doped films decreased owing to enhanced filling of the voids from the decreasing viscosity while the R_a roughness of the Ga-doped films decreased owing to enhanced coverage of the substrate surface by the increasing viscosity. The leveling of the R_a roughness at the highest Mn dopant level is attributed to void filling with 5MC and 9MC. This leveling was not observed with Ga doping owing to the reduced tendency to fill voids from the overlay effect of the greater viscosity.

Figure S1, Supporting Information, reveals that increasing the Ga dopant concentration reduced the extent of wetting while all of the Mn dopant concentrations readily wet the substrates. These data confirm the previous comments about the effects of the viscosity differences between the two dopant systems on the physical processes of coating.

The glancing angle X-ray diffraction (GAXRD) data indicate (graphs previously published^[65]) that Ga₂O₃ is highly soluble in CeO₂ because no Ga₂O₃ was detected. The low GAXRD peak intensities (not shown) indicate that Ga₂O₃ destabilized the CeO₂ structure but it still enhanced the gel → crystalline conversion, probably by acting as a nucleating agent. In contrast, the solubility of Mn in CeO₂ was lower than for Ga₂O₃, as evidenced by the

precipitation of Mn₃O₄ with 5MC and 9MC. It is uncertain whether the nondetection of Mn₃O₄ resulted from its dissolution or its precipitation at a level below the limit of detection of the instrument (typically ≈1 vol%^[66]). However, the higher GAXRD peak intensities (not shown) for all of the Mn-doped samples than those for the CeO₂-coated samples is a clear indication of Mn dissolving and enhancing recrystallization. This is emphasized by the greater extent of crystallinity of these samples compared to the Ga-doped samples. Further, it appears that this effect was maximized for 5MC, suggesting saturation solubility in the range 1–5 mol% Mn and supersaturation and consequent structural destabilization at 9 mol% Mn. These differential solubilities may reflect not only intrinsic behavior but they also may reflect the extrinsic effect of precursor viscosity and consequent intimacy of interfacial contact area.

Table 1 also shows that Mn doping resulted in the formation of rutile. This probably resulted from the dual effect of superior wetting and chemical attack of the Ti by the nitrate(s), which oxidized during calcination at 650 °C.

The X-ray photoelectron spectroscopy (XPS) analyses, which are shown for the dopants in Figure S2, Supporting Information, and summarized for all species in **Table 2**, reveal that Ga³⁺, Mn²⁺, Mn³⁺, and Mn⁴⁺ were detected. These data, in conjunction with the GAXRD data, confirm the dissolution of Ga in CeO₂ as well as that of Mn⁴⁺ in CeO₂; it is uncertain if the identification of Mn²⁺ and Mn³⁺ is a result of their presence as solutes in CeO₂, as precipitated Mn₃O₄ (MnO·Mn₂O₃), or both. Also, it is possible that the detection of Mn²⁺ resulted from the presence of MnO but this was not confirmed by GAXRD. As the XPS beam (10 μm Ø^[67]) scanned a large area and the Mn₃O₄ was present as a minor phase, it is likely that the XPS data reflect soluble Mn.

Table 1. Relative proportions of thin film phases based on maximal GAXRD peak heights.

Sample	Phase			
	Major	Substantial	Minor	Trace
Uncoated	α-Ti	–	–	–
CeO ₂ -coated	α-Ti	CeO ₂	–	–
1GC	α-Ti	–	–	–
	CeO ₂			
5GC	CeO ₂	α-Ti	–	–
9GC	CeO ₂	–	α-Ti	–
1MC	α-Ti	CeO ₂ (–)	α-Mn ₃ O ₄	–
5MC	α-Ti	CeO ₂ (+)	Rutile	–
			α-Mn ₃ O ₄	
9MC	α-Ti	–	CeO ₂	–
			Rutile	
			α-Mn ₃ O ₄	

Table 2. Identification of ions and valences based on XPS spectra.

Sample	Phase				
	Ce ³⁺ /Ce ⁴⁺	Ga ³⁺	Mn ²⁺ /Mn ³⁺	Mn ³⁺	Mn ⁴⁺
CeO ₂ -coated	✓	–	–	–	–
1GC	✓	✓	–	–	–
5GC	✓	✓	–	–	–
9GC	✓	✓	–	–	–
1MC	✓	–	–	✓	(✓)
5MC	✓	–	✓	✓	✓
9MC	✓	–	✓	✓	✓

It should be noted that the valences indicated in these Equations are not integral valences but fractional valences that are reflected in XPS peak shifts. These fractional shifts are observed commonly in XPS^[68] and can be explained by electro-negativity (Figure S3, Supporting Information).

2.2.1. Doped versus Undoped

As the sol–gel precursor was Mn(NO₃)₂·4H₂O (i.e., Mn²⁺), then it is likely that the conversion to Mn³⁺ and/or Mn⁴⁺ resulted from intervalence charge transfer (IVCT)^[69–71] according to



Consequently, Mn solubility can enhance the Ce redox to increase the [Ce³⁺]. However, this also is the case for Ga doping, which suggests the IVCT reaction



Although an integral valence of Ga⁴⁺ is known in biological systems,^[72,73] it is not cited generally for inorganic systems; fractional changes in valence from XPS data are observed commonly.

2.2.2. Undoped Films

Table S4, Supporting Information, reveals that the surface [Ce³⁺] is 17 at% but the subsurface [Ce³⁺] is ≈26 at%. As surfaces are associated with broken bonds and associated oxygen vacancies,^[74] while the subsurface and bulk reflect lattice bonding, these data are the reverse of those expected. As there are no dopants present, then the only possible means of enhancing the subsurface [Ce³⁺] is interaction with the substrate. Here, the Ce³⁺ ions at the surface are exposed to two interfaces, these being air/Ce and Ti/Ce, while the Ce³⁺ ions at the subsurface are exposed only to the air/Ce interface. The equilibria at the substrate/coating interface suggest the reaction



Further, there is the possibility of IVCT through the following exchange reactions



The potential to form Ti⁴⁺ is supported by the fact that 1) the samples were heated in air at 650 °C for 2 h, which could have caused oxidation from air; 2) Ti is well known as a strong reducing agent,^[75] which could remove oxygen from CeO₂ (Equation (4) and (5)); and 3) the detection of rutile in all of the Mn-doped films (Table 1), although the more-protected Ga-doped and the less-protected CeO₂-coated samples (Figure 1) exhibited no rutile.

2.2.3. Ga Doping

The XPS data for the changes in concentrations upon Ga doping are provided in Figure S2 and S4 and Table S4, Supporting Information. These data are plotted for the surface ([Ce³⁺] in **Figure 2**; these data are relative to the initial (baseline) [Ce³⁺] (viz., [Ce³⁺]/([Ce³⁺] + [Ce⁴⁺])) of 17% for undoped CeO₂ in order to show the changes caused by doping. These data show that Ga doping resulted in an initial increase in [Ce³⁺] (1 mol%). The reason for this has been elucidated elsewhere,^[69,76] where inhomogeneously distributed dopants at low concentrations destabilize the lattice by inhibiting recrystallization and grain growth and by introducing structural defects. This is confirmed by the GAXRD peak intensities for CeO_{2-x} (not shown), which increase with increasing Ga dopant level (Table 1), thus revealing slightly increasing crystallinity. However, more importantly increasing the Ga dopant levels to 5 mol% and 9 mol% consistently decreased [Ce³⁺].

These data must be interpreted in light of the potential solid solubility and charge compensation mechanisms using Kröger–Vink notation,^[77] which are given in Text S1 in the Supplementary Information.

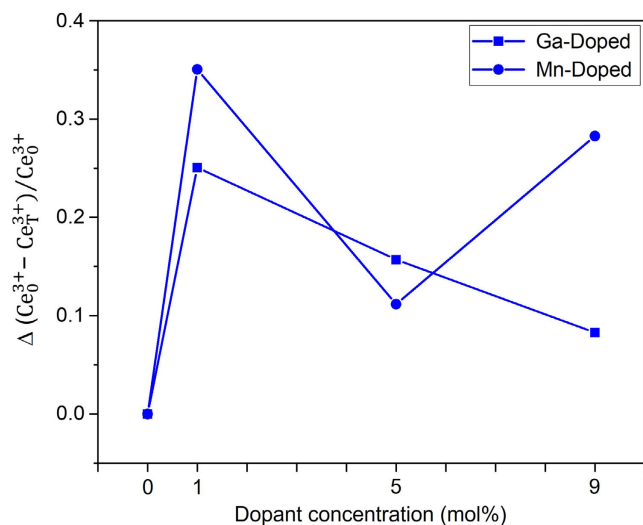


Figure 2. XPS data for effects of Ga and Mn doping in terms of changes in $[Ce^{3+}]$ relative to the baseline undoped value of 17%; subscripts: 0 = undoped, T = doped.

However, the data in Table S4, Supporting Information, are critical in that they decouple the concentrations of Ce and O at the outermost surface layer ($[Ce^{3+}]$ and $[Ce^{4+}]$), where there are terminating bonds, and the underlying layer (subsurface $[Ce^{3+}-O]$ and $[Ce^{4+}-O]$), where there are lattice bonds. These data for the three doped samples can be examined stepwise to determine the operating mechanisms: 1) Ga doping enriched the surface with Ce (viz., Ce^x , which is Ce migrated to the surface in response to dopant addition), which could result from both substitutional solid solubility/ionic charge compensation (Equation S1, Supporting Information), substitutional solid solubility/electronic charge compensation (Equation S2, Supporting Information), or interstitial solid solubility/ionic charge compensation (Equation S4, Supporting Information). 2) The surface also was enriched with oxygen, which means that both solubility mechanisms are possible but charge compensation must be electronic (Equation S4 and S5, Supporting Information) and/or by redox (Equation S3 and S6, Supporting Information). 3) The change in $[Ce^{3+}]$ eliminates electronic charge compensation (Equation S(2) and S(5), Supporting Information) from consideration because this mechanism does not alter the Ce valence. 4) As the preceding requires redox charge compensation, the change in $[Ce^{3+}]$ also eliminates interstitial solid solubility/ionic charge compensation (Equation S(4), Supporting Information) from consideration. 5) The decreasing $[Ce^{3+}]$ with Ga doping could result only from substitutional solid solubility/redox (oxidation) charge compensation (Equation S(3), Supporting Information). 6) As the source of oxygen enrichment is O_2 (g), then it is highly unlikely that substitutional solid solubility/ionic charge compensation (Equation S(1), Supporting Information) is possible because the V_O^\bullet formed in this mechanism would be annihilated. 7) As Equation (S1, S2, and S4–S6), Supporting Information, have been eliminated owing to inconsistency with the data in Table S4, Supporting Information, then the operating mechanism is substitutional solid solubility/redox

charge compensation (Equation (S3), Supporting Information); 8) Figure S2a–c, Supporting Information, shows that the Ga valence increased with Ga doping, which is explained by the IVCT exchange reaction ($Ce^{4+} \rightarrow Ce^{3+}$ reduction) in Equation (6). Consequently, this partially offsets the $Ce^{3+} \rightarrow Ce^{4+}$ oxidation in Equation S3, Supporting Information, which explains why the changes in $[Ce^{3+}]$ are less than expected from the changes (i.e., doping levels) in $[Ga^{3+}]$. 9) Electronegativity plays an insignificant role as this would cause the Ga valence to decrease, which is not the case.

The preceding discussion demonstrates the following for the Ga-doped CeO_2 thin films: 1) The solubility mechanism is substitutional solid solubility. 2) Charge compensation is by $Ce^{3+} \rightarrow Ce^{4+}$ oxidation, thereby decreasing $[Ce^{3+}]$. 3) $Ce^{4+} \rightarrow Ce^{3+}$ reduction from IVCT partly reverses this trend by increasing the $[Ce^{3+}]$. 4) The decreasing $[Ce^{3+}]$ with increasing $[Ga^{3+}]$ indicates that the dominant mechanism is redox charge compensation, not IVCT. and 5) Electronegativity plays little or no role in these effects.

2.2.4. Mn Doping

The XPS data for the changes in concentrations upon Mn doping are provided in Figure S2 and Table S4, Supporting Information. These data are plotted for the surface ($[Ce^{3+}]$ in Figure 2; these data are relative to the initial (baseline) $[Ce^{3+}]$ (viz., $[Ce^{3+}]/([Ce^{3+}] + [Ce^{4+}])$ of 17% for undoped CeO_2 in order to show the changes caused by doping. These data show that Mn doping resulted in an initial increase in $[Ce^{3+}]$, followed by a significant decrease in $[Ce^{3+}]$ for 5MC and then a significant increase for 9MC (but not to the level of 1MC). For the three doped samples, these specific data suggest that the solubility mechanism is the same as for Ga doping because the general trends are the same. However, closer examination of the data reveal significant differences in trends for the two dopants for [Ce], [O], and $[Ce^{3+}]$, so this assumption may be incorrect. The possible defect equilibria are given in Text S1, Supporting Information.

Again, the only mechanism capable of decreasing the $[Ce^{3+}]$ overall is Equation (S9), Supporting Information, which illustrates substitutional solid solubility and redox charge compensation. However, the XPS data show that Mn doping resulted in Mn valence increase, so the IVCT exchange reactions ($Ce^{4+} \rightarrow Ce^{3+}$ reduction) in Equation (1 and 2) would offset the decreasing the $[Ce^{3+}]$. The situation is complicated by other IVCT possibilities



In effect, decoupling the solid solubility, charge compensation, IVCT, and electronegativity mechanisms is complicated by the inflection in the data for the three Mn-doped samples. It is noted that the trends for [Ce] and $[Ce^{3+}]$ for 1MC and 5MC are identical to those for Ga doping but the reverse trend for [O] (viz., a decrease) is the case. This can be interpreted in terms of substitutional solid solubility/ionic charge compensation (Equation S(7), Supporting Information), which generates

V_{O} . However, this trend is reversed for 9MC, so it is not considered to be likely. Further, the $[\text{Ce}]$ decrease for 9MC cannot be explained by conventional considerations. These inconsistencies suggest the influence of another mechanism beyond the present considerations.

The XPS data in Figure S2, Supporting Information, and in Figure 2 differ somewhat from those for Ga doping: 1) 5MC: $[\text{Ce}^{3+}]$ decreases and the valences of Mn^{3+} and Mn^{4+} decrease (any change in Mn^{2+} is unknown). These data are consistent with Equation (7) and (8) in the forward direction. 2) 9MC: $[\text{Ce}^{3+}]$ increases and the valences of Mn^{2+} , Mn^{3+} , and Mn^{4+} increase. These data are consistent with Equation (7–9) in the reverse direction.

The relevant electronegativities for Mn^{2+} (1.50), Mn^{3+} (1.85), and Mn^{4+} (unknown but >1.85) compared to those of Ce^{4+} (1.50) and Ce^{3+} (1.15)^[78] indicate that the valences of Mn should decrease, which is consistent with 5MC but not 9MC. Again, this indicates the influence of another mechanism. Consequently, it is concluded that the charge compensation mechanism is not ionic (Equation S7, Supporting Information) but redox (Equation S9, Supporting Information) and that this may be altered by the effects of IVCT and electronegativity. In conclusion: 1) The solubility mechanism is substitutional. 2) For 5 mol% Mn: a) charge compensation is by redox through $\text{Ce}^{3+} \rightarrow \text{Ce}^{4+}$ oxidation (Ce valence increase), thereby decreasing $[\text{Ce}^{3+}]$; b) IVCT enhances this Ce oxidation effect and decreases the valence of Mn; and c) electronegativity contributes to these effects. 3) For 9 mol% Mn: a) at the highest dopant level, the system becomes effectively overdoped and saturates the substitutional sites, thereby initiating interstitial solid solubility. Dual solubility mechanisms have been observed before.^[79] Charge compensation then is dominated by redox through $\text{Ce}^{4+} \rightarrow \text{Ce}^{3+}$ reduction (Equation S(12), Supporting Information), thereby increasing $[\text{Ce}^{3+}]$; b) IVCT should enhance Ce oxidation and Mn reduction (Equation (7–9) in the forward direction) but these are not the case. Hence, IVCT enhances the reduction effect and so is consistent with Equation (7–9) in the reverse direction; and c) electronegativity should enhance

Ce oxidation and Mn reduction but these are not the case, so its role is minimal.

2.2.5. Surface versus Subsurface

Figure S4 and Table S4, Supporting Information, show that the values of the surface $[\text{Ce}^{3+}]$ were uniformly higher for all doped films compared to that of the CeO_2 -coated substrate. However, while increasing $[\text{Ga}]$ decreased the surface $[\text{Ce}^{3+}]$, the trend for $[\text{Mn}]$ revealed a minimum in the surface $[\text{Ce}^{3+}]$. With the exception of this minimum, the surface $[\text{Ce}^{3+}]$ values for the Mn-doped films were the highest of all samples.

The data for the subsurface $[\text{Ce}^{3+}]$ are a reflection of 1) the difference between the broken bonds at the surface (increasing the $[\text{Ce}^{3+}]$) versus the underlying lattice bonds (decreasing the $[\text{Ce}^{3+}]$); 2) dilution from the presence of dopant oxide surface precipitates; 3) dopant concentration gradient into the film; and 4) interaction between the film and substrate. The last effect is likely to be responsible for the instances where subsurface $[\text{Ce}^{3+}] > \text{surface } [\text{Ce}^{3+}]$. For the other three films, the first effect probably is responsible for surface $[\text{Ce}^{3+}] > \text{subsurface } [\text{Ce}^{3+}]$. While 5GC and 9GC are compositionally similar, the same trend for 5MC is likely to be the case because Table 1 shows that this film exhibited the highest CeO_2 proportion.

2.2.6. Biological Analyses

Figure 3 summarizes the potential biological responses to the relevant ions Ti, Ce, Ga, and Mn. Ti has been observed to favor osteoblast attachment, differentiation, and hence bone regeneration; it also has exhibited minimization of bacterial growth.^[80–84] Ce is known to regulate the proliferation and differentiation of osteoblasts as well as promote hydroxyapatite (HA) precipitation.^[85–88] Like Ti, Ce is a catalyst that can inhibit bacterial proliferation; Ce also exhibits anti-inflammatory capabilities.^[37,89,90] Ga has been reported to show antibacterial activity as well as osteoblast proliferation and osteoclast minimization

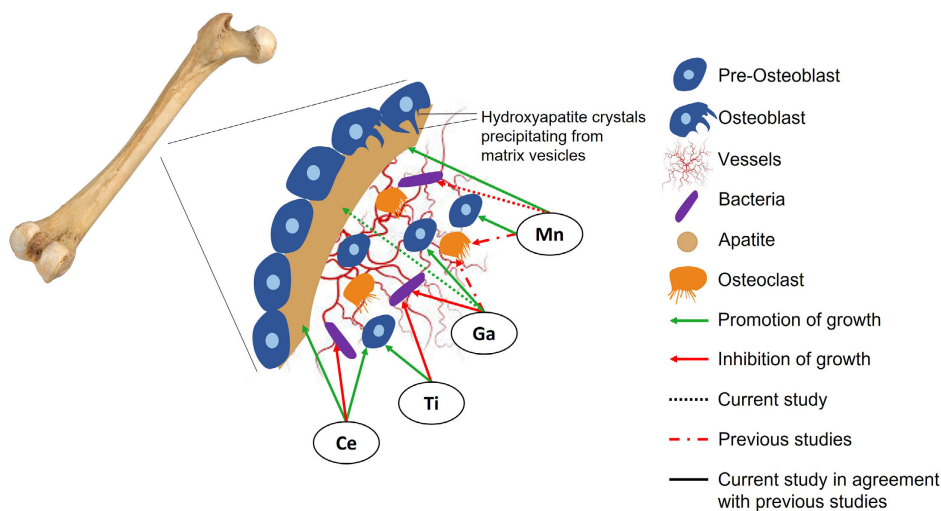


Figure 3. Schematic of biological responses to bioactive ions. Reproduced (adapted) with permission from publisher (22 April 2022), Springer International Publishing, Switzerland (2016).^[97,98]

capabilities.^[59,91–93] In common with the other ions, Mn is a biologically active ion and it can enhance osteoblast adhesion, differentiation, and mineralization as well as provide antibacterial properties.^[61,94–96] While the present work confirms the bioactivities of these ions, it also reveals that Ga enhances hydroxyapatite precipitation upon exposure to simulated body fluid (SBF) and Mn has the capacity kill both *S. aureus* and *E. coli*.

2.3. Antibacterial Assays

Figure 4 shows the percentage reduction in the number of live bacteria released from the materials in the presence of CeO₂ films with varying Ga doping (Figure 4a) and Mn doping (Figure 4b) levels, varying Ga doping (Figure 4c) and Mn doping (Figure 4d) levels with respect to the uncoated (control) samples. Each point represents the mean number of viable counts for three samples. The error bars give the standard deviations. The bacterial survival percentages are given in Figure 4e.

All the undoped and Ga-doped samples have the antibacterial performances higher than ≈86% against both *S. aureus* and *E. coli* but the individual data are not statistically distinguishable (Figure 4). This effectiveness may reflect the chemical similarities between Ga³⁺ and Fe³⁺ and the bacterial inability to differentiate these ions in the relevant metabolic processes.^[99] Considering only the average values in Figure 4a, the following trends are suggested: 1) The thin films generally were more effective in killing *S. aureus* than *E. coli*, although 9GC was a clear exception. 2) Increasing Ga doping levels generally increased the bactericidal effects for both bacteria, although 9GC again was a clear exception. 3) There was little difference in the bactericidal effects against *S. aureus* between the uncoated control and the CeO₂-coated samples, with 9GC again being an exception. 4) There was a greater improvement in bactericidal effects against *E. coli* between the uncoated control and the CeO₂-coated samples. 5) The only statistically significant difference ($p < 0.001$) was the greater bactericidal effect against *E. coli* for 9GC (94.8%) relative to the uncoated control (90.4%).

Figure 4b reveals that all the Mn-doped samples exhibit antibacterial performances greater than ≈92% against both *S. aureus* and *E. coli* with two statistically distinguishable data pairs. Again, considering just the averages, the following trends are suggested: 1) The thin films generally were more effective in killing *S. aureus* than *E. coli*. 2) Increasing Mn doping levels generally increased the bactericidal effects for *S. aureus* at significant differences ($p < 0.01$) for both 5MC and 9MC relative to 1MC, although the bactericidal activity against *E. coli* remained unchanged with increasing Mn level. 3) There were significant differences ($p < 0.01$) in the bactericidal effects against *E. coli* between the uncoated sample and all of the Mn-doped samples. 4) There was a slight improvement in bactericidal effects against *E. coli* for the Mn-doped samples relative to the CeO₂-coated sample.

Figure 5c,d shows the percentages of bacteria adhered to the surfaces of the samples relative to that of the uncoated sample. All the samples revealed significant improvements in bactericidal activity against both *S. aureus* and *E. coli* relative to the uncoated sample. Again, considering only the averages, the following trends are suggested: 1) Relative to the uncoated sample, the bactericidal activity of the samples against both *S. aureus* and *E. coli*

was enhanced, although *E. coli* showed a lower affinity toward the GC-doped samples compared to that of *S. aureus*. 2) Increasing the Ga dopant level decreased the bacterial adhesion for both *S. aureus* and *E. coli*; 9GC exhibited the best performances against both bacteria. 3) All of the samples revealed statistically significant differences ($p < 0.0001$) relative to the uncoated sample except for the CeO₂-coated sample against *S. aureus* and 1GC ($p < 0.01$) and 5GC ($p < 0.05$) against *S. aureus*. 4) The MC-doped samples revealed a trend opposite to that of the GC-doped samples, where the former exhibited superior antibacterial performance against *S. aureus*. 5) With increasing MC doping, the bacterial adhesion decreased significantly relative the uncoated sample ($p < 0.0001$), although 1MC was slightly out of trend ($p < 0.001$). 6) With increasing MC doping, the bacterial adhesions showed reverse trends for the two bacteria, where *S. aureus* decreased and *E. coli* increased.

The survival percentages of the bacteria, shown in Figure 4e, were calculated according to

$$\frac{\text{CFU}_{24\text{h}}}{\text{CFU}_{0\text{h}}} \times 100 \quad (10)$$

where CFU_{24 h} is the number of colonies of surviving bacteria on the sample after 24 h incubation and CFU_{0 h} is the number of colonies of bacteria before incubation.

The data for the uncoated and CeO₂-coated samples show that, in common with other comparative studies,^[100–102] the killing of gram-positive *S. aureus* was more effective than that of gram-negative *E. coli*, suggesting that both the substrate and CeO₂ coating were negatively charged.

Plakhova et al.^[103] have shown that the isoelectric point of CeO₂ is at pH 6.3, where more acidic conditions establish a positive surface charge (viz., Ce⁴⁺) and more basic conditions establish a negative surface charge (viz., Ce³⁺).

The data for the uncoated and CeO₂-coated samples also show that CeO₂ coating causes the surfaces to become less negatively charged, where the killing of gram-positive *S. aureus* was less effective by the substrate but the killing of gram-negative *E. coli* by the substrate was more effective.

With Ga doping and gram-positive *S. aureus*: While Ga doping caused both the roughnesses and [Ce³⁺] to decrease, the bacterial survival percentages relative to the CeO₂-coated sample were not consistent, decreasing for 1GC and 5GC and increasing for 9GC. This is interpreted in terms of three variables. For 1GC, Figure S1, Supporting Information, and the roughness data in Figure 1f indicate that the negatively charged Ti alloy asperities^[104] provide the dominant effect. For 5GC, the same data indicate again that the roughness and Ti alloy surface charge are relevant but that the former provides the dominant effect. For 9GC, which exhibited the greatest coverage of the Ti alloy substrate, the significant increase and reversal in trend in bacterial survival percentages for gram-positive *S. aureus* are consistent with the dominant roles of negatively charged Ce³⁺, where the [Ce³⁺] was the lowest value for the doped samples (Table S4, Supporting Information).

With Ga doping and gram-negative *E. coli*: In comparison to the CeO₂-coated sample, the bacterial survival percentages for the gram-negative *E. coli* were only slightly changed for 1GC and 5GC, suggesting only minor if any effect of roughnesses, [Ce³⁺], and Ti alloy asperities. However, for 9GC,

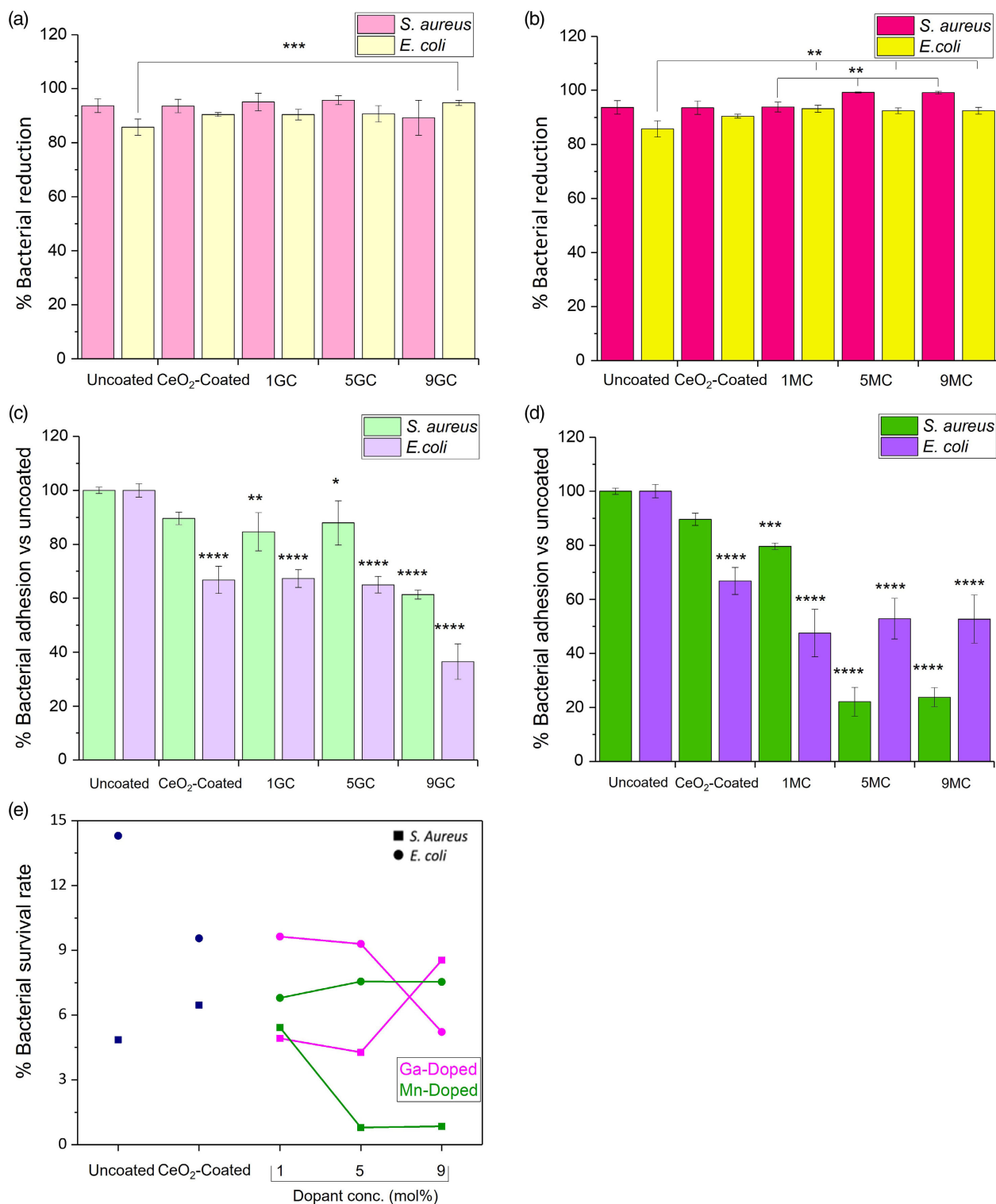


Figure 4. *S. aureus* and *E. coli* bacterial reduction: a) Ga-doped samples, b) Mn-doped samples, *S. aureus* and *E. coli* bacterial adhesion (relative to control (uncoated sample): c) Ga-doped samples, d) Mn-doped samples, e) *S. aureus* and *E. coli* bacterial survival percentages after 24 h incubation (bacterial concentration = CFU mL⁻¹; **p* < 0.05, ***p* < 0.01, ****p* < 0.001, and *****p* < 0.0001).

the bacterial survival percentages for gram-negative *E. coli* was decreased significantly, suggesting that the low roughness and

low [Ce³⁺] are relevant. In light of the similarities in trends in bacterial survival percentages for the Mn-doped samples

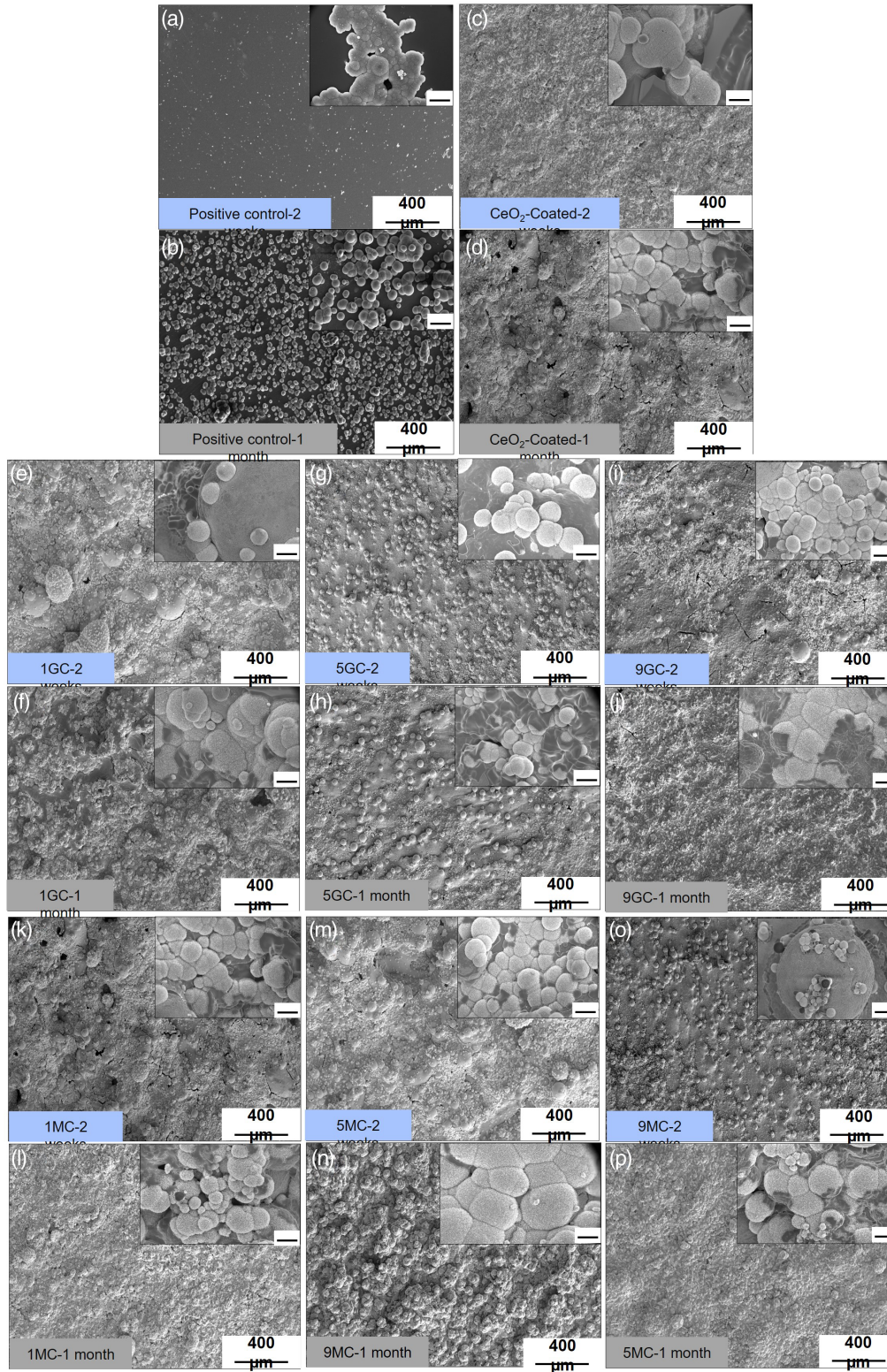


Figure 5. FESEM images of HA precipitation after immersion in SBF for 2 weeks or 1 month: a,b) positive control, c,d) CeO₂-coated, e,f) 1GC, g,h) 5GC, i,j) 9GC, k,l) 1MC, m,n) 5MC, o,p) 9MC; calcined at 650 °C (insets: 10 μm scale bar).

(discussed subsequently), it is probable that the [Ce³⁺] provides the dominant effect.

With Mn doping and gram-positive *S. aureus*: The bacterial survival percentages relative to the CeO₂-coated sample were

decreased significantly. Critically, they correlate closely with both the roughnesses (Figure 1f) but they exhibit a reverse correlation with $[Ce^{3+}]$ (Table S4, Supporting Information), where the negative Ce^{3+} surface would be expected to kill gram-positive *S. aureus* but the opposite occurred. Consequently, the direct role of the roughness is indicated. However, Mn_3O_4 was present in increasing amounts with increasing $[Mn]$ as a precipitate in all three samples. Although this precipitation is a reflection of the defect equilibria, the presence of the precipitates is considered an independent variable that is deleterious to bacterial survival, although this effect is minor.

With Mn doping and gram-negative *E. coli*: In comparison to the CeO_2 -coated sample, the bacterial survival percentages for the gram-negative *E. coli* also were decreased, which indicates that the surface charge through the $[Ce^{3+}]$ does not provide the dominant effect. The bacterial survival also does not correlate with the roughness (Figure 1f), so this also is not a dominant effect. In contrast, the slight increase in bacterial survival correlates with the Mn_3O_4 precipitation (Table 1), which is consistent with its negative surface charge.^[105,106]

The last point is not surprising because both sample roughness and wetting also influence the bacterial response. However, the importance of the role of $Ce^{4+} \leftrightarrow Ce^{3+}$ redox and V_O^\bullet generation in the formation and elimination of ROS is well known.^[107] Hence, the initiation of the mechanism of the killing of *S. aureus* and *E. coli* is suggested by the IVCT process indicated in Equation (1–3) and (7–9), which provides the means by which Ga and Mn doping cause the $Ce^{3+} \leftrightarrow Ce^{4+}$ redox, as well as the direct generation of V_O^\bullet indicated by Equation (S4 and S7), Supporting Information. Perhaps more significantly, these analyses suggest the significant role of the $[Ce^{3+}]$ in the homogeneous Ga-doped CeO_2 solid solutions and how small changes of as little as 1 at% can exert a very dominant effect on bacterial survival percentages. In contrast, for the inhomogeneous Mn-doped samples, all three main factors appear to play roles simultaneously.

In addition to the three discussed variables of roughnesses, $[Ce^{3+}]$, and Ti alloy asperities, the fourth variable of the $[Ga]$ or $[Mn]$ also must be considered. The data in Figure 4e indicate that there is no clear correlation between bacterial survival percentages and dopant concentration. If this were the case, then similar general trends for both gram-positive and gram-negative bacteria, which was not the case. In fact, opposite trends

generally were observed. Further, Table S2, Supporting Information, shows that both ions are known to exhibit antibacterial activity, so only decreasing trends in survival percentages would be expected, again not the case. Consequently, this variable cannot be decoupled from the other three. However, in the case of Ga doping, the effectively mirror images of the trends suggest the critical role of $[Ce^{3+}]$. In the case of Mn doping, the absence of parallel or mirror image trends is indicative of the contributions of multiple effects, although the $[Mn]$ does not appear to be dominant.

2.4. Acellular Mineralization (Apatite Formation)

The outcomes of the investigation of the capacity of the samples to facilitate HA formation in vitro by immersion in SBF are revealed in the GAXRD patterns of Figure S5, Supporting Information; these data are summarized in Table 3. FESEM images after immersion in SBF for 2 weeks and 1 month are shown in Figure 5. The main conclusions from these data are as follows:

2.5. CeO_2 -Coated

The reversal in the major phase from CeO_2 (2 weeks) to α -Ti suggests that, in the absence of HA peaks, 1) amorphous HA preferential precipitates on the α -Ti and/or 2) SBF enhances the precipitation of CeO_2 . Although the FESEM images (Figure 6a–d) confirm the formation of HA, the absence of a hump at $\approx 32^\circ 2\theta$ in the GAXRD data (Figure S5a, Supporting Information) suggests that the former is the case.

2.6. Ga-Doped (1GC, 5GC, 9GC)

1GC shows attenuation the GAXRD intensities for both CeO_2 and α -Ti, again in the absence of HA peaks. There also is an unidentified peak at $\approx 45^\circ 2\theta$, which does not correspond to any Ce-based or Ti-based phases or Ce titanites. The observation of HA in the FESEM images (Figure 6e, f), in conjunction with the GAXRD data, supports the view that amorphous HA precipitates on both phases. This indicates that Ga doping at this low level enhances HA precipitation on CeO_2 .

5GC at only 1 month shows the maximal HA (211) peak only. It is unexpected that no peaks of minor intensity are apparent.

Table 3. Relative proportions of thin film phases following soaking in SBF based on maximal GAXRD peak heights.

Sample	Phase							
	Major		Substantial		Minor		Trace	
	2 weeks	1 month	2 weeks	1 month	2 weeks	1 month	2 weeks	1 month
CeO_2 -coated	CeO_2	α -Ti	α -Ti	CeO_2	–	–	Unknown	–
1GC	α -Ti	α -Ti	CeO_2	CeO_2	–	–	–	–
5GC	CeO_2	HA	α -Ti	–	–	CeO_2 α -Ti	–	–
9GC	HA	HA	–	–	α -Ti	CeO_2	–	α -Ti Unknown
1MC	CeO_2 α -Ti	HA	–	–	HA	CeO_2	–	α -Ti
5MC	CeO_2 α -Ti	HA	Amorphous	CeO_2 α -Ti Anatase	–	–	–	–
9MC	α -Ti	α -Ti	–	–	HA CeO_2	CeO_2 HA	–	–

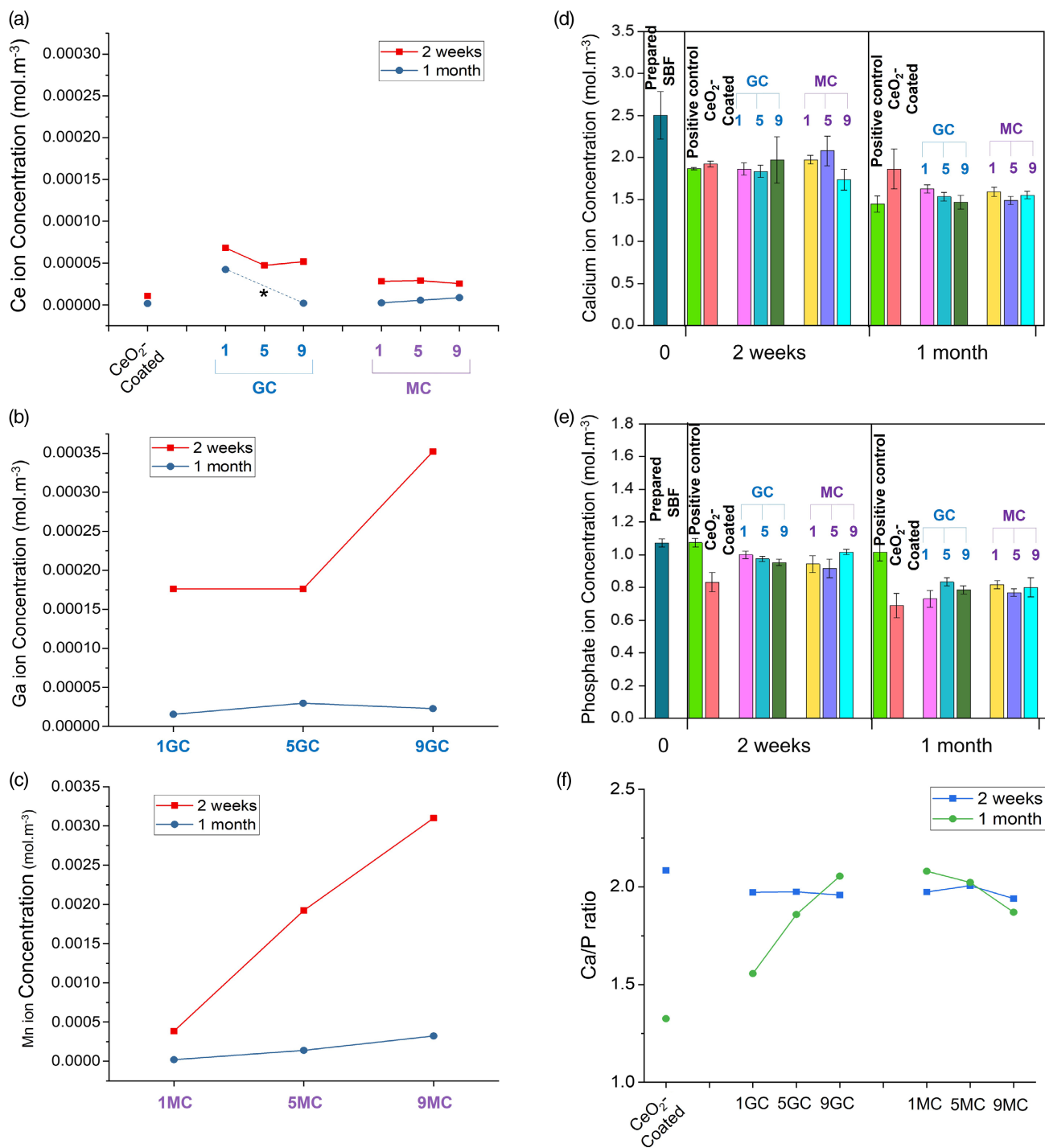


Figure 6. ICP-OES results for ionic concentrations of residual SBF after immersion for 2 weeks or 1 month: a) Ce, b) Ga, c) Mn (single-point data) and d) Ca, e) P (multiple-point data), f) Ca/P ratio; calcined at 650 °C for 2 h (* for 5GC (a) was off-scale).

Although this could be a result of preferred orientation, the (211) generally does not exhibit this.^[108] However, it is known that increasing crystallinity increases the intensity of the (211) while the intensities of the neighboring strong (112) and (300) peaks decrease.^[109] However, it is most likely that the single HA peak observed on these uneven samples is not the (211) peak (31.8° 2θ)

but the (300) peak (32.9° 2θ), which is known to occur with little indication of minor peaks.^[110] The range of locations of this peak in the present work was 31.50° – 33.03° 2θ. As the peak intensities of α-Ti increased but those of CeO₂ decreased, this supports the conclusion that Ga doping enhances HA precipitation on CeO₂. However, the role of time in increasing precipitation is

clear. The FESEM images (Figure 5g, h) reveal the precipitation of HA at both 2 weeks and 1 month (at greater levels than for 1GC), so the former would involve amorphous HA and the latter crystalline HA.

9GC at both 2 weeks and 1 month shows that the amount of Ga doping is relevant in that increasing [Ga] increases the extent of HA precipitation. The ready precipitation at this [Ga] results in peak intensity decreases for both α -Ti and CeO₂. What appears to be the same unidentified peak at $\approx 45^\circ 2\theta$ is present. The FESEM images (Figure 5i, j) reveal high levels of HA, which confirms the effect of both [Ga] and time in enhancing HA precipitation. However, as with 1GC and 5GC, the extent of coverage of the surface by HA is incomplete.

2.7. Mn-Doped (1MC, 5MC, 9MC)

1MC reveals low GAXRD intensities (Figure S5f, Supporting Information) and the FESEM images show a high level of coverage by HA (Figure 5k). These data confirm that precipitated HA is amorphous and that time converts it to crystalline. This is a well-known phenomenon, where the amorphous precipitation is known as amorphous calcium phosphate (ACP).^[111–113]

5MC at 2 weeks is similar to 1MC at the same time point both in terms of mineralogy (Figure S5g) and microstructure (Figure 5m). However, at 1 month, the results are completely different. These data reveal the presence of well crystallized HA and anatase; the GAXRD peak intensities for CeO₂ and α -Ti also are increased. There also is a broad amorphous hump centered under the HA peak. These results are interpreted in terms of attenuation of the GAXRD peak intensities by amorphous HA (Figure 5n), its increased crystallinity over time (Figure S5g, Supporting Information), and increased exposure of the underlying substrate owing to decreased volume and shrinkage of HA upon recrystallization. Although the location of the amorphous hump would suggest that it is HA, this is not supported by its absence in all other GAXRD patterns and the decrease in amorphous HA at 1 month. Consequently, this amorphous phase remains unidentified. The cause of formation of anatase also remains unknown. In light of the number of anomalies that are not consistent with other samples, it is concluded that this sample is not representative of the phenomena and that this probably lies in an unknown processing variation.

9MC at both 2 weeks and 1 month reveal the negative impact of the [Mn] on the precipitation of HA (Figure S5h, Supporting Information); this is confirmed by the microstructures (Figure 5o,p), which indicate a lower HA distribution density than for 5MC.

The preceding discussion leads to the conclusions that precipitation is enhanced by increasing [Ga], decreasing [Mn] concentration (but not nil [Mn]), and increasing time.

Another factor that may be relevant is the surface roughness, which has been observed before, where the asperities provide high-surface-energy nucleation sites for HA precipitation.^[114] However, comparison with the roughness data in Figure 1f reveals no apparent correlation.

Another possible factor investigated in the present work is the [Ce³⁺] values, which are shown in Figure 2. These data show that, for the doped samples, increasing [Ga] and [Mn] both decrease

[Ce³⁺]. However, the GAXRD data (Figure S5c–h, Supporting Information) show that increasing [Ga] in these homogeneous solid solutions enhanced HA formation but increasing [Mn] in these inhomogeneous samples had the reverse effect. From this, it is concluded that [Ga] and HA formation were inversely proportional, where the Ce³⁺ acts as a nucleation site, but that this effect was not observed in the Mn-doped samples owing to their inhomogeneity and lower solubility levels, as evidenced by the formation of precipitates.

2.8. SBF

The interaction of the films with SBF was investigated by analyzing the residual solutions after film immersion for 2 weeks and 1 month. The [Ce], [Ga], and [Mn] are shown in Figure 7a–c, respectively. These data show that Ce is only slightly soluble in SBF, which has been observed before.^[115] Both Ga and Mn show increasing solubilities of the dopant ions with increasing dopant concentrations, which is expected. However, Ga is considerably more soluble, which also has been noted previously.^[116] Figure 6b shows that the solubility of Ga increased significantly with time, which is consistent with the GAXRD data in Figure S5c–e, Supporting Information. That is, increasing coverage by HA over time reduced the free film surface subject to leaching by SBF and the corresponding Ga solubility. The Mn solubility, which has been observed before,^[117–119] is substantially less than that of Ga, decreasing only slightly over time. The GAXRD data for 9MC in Figure S5h, Supporting Information, show that crystalline HA is present at a low level and the FESEM data. The probable reason for this is that examination of Figure S5f–h, Supporting Information, for 2 weeks immersion shows that the amount of HA was significant only for 9MC while the converse was the case for 1 month immersion. These trends suggest that the apparently anomalous data in Figure 6c result from the initial blockage by HA after 2 weeks immersion and deterioration of the HA (from the high [Mn]) after 1 month immersion.

Figure 6a confirms the anomalous nature of 5GC by the observation that the [Ce] for this sample was off-scale.

Figure 6d,e contrasts the initial [Ca] and [P] with those after immersion for the undoped and doped films; the data for the positive control also are included.

2.8.1. Positive Control

These data appear to be anomalous in that, while the [Ca] exhibited the expected decrease with immersion, the [P] remained effectively unchanged. The positive control was Unigraft, which is a bioactive and resorbable bioglass with principal components Ca, P, and Si. The explanation for this lies in the FESEM images, which show highly agglomerated particles after 2 weeks immersion but individual and slightly agglomerated particles of the same (individual) grain size after 1 month immersion. These images indicate that the resorbable bioglass was deagglomerated over time, suggesting resorption by the SBF. Consequently, there are two competing diffusion mechanisms, where HA formation diffuses Ca and P to the bioglass and bioglass resorption diffuses Ca and P into the SBF. Figure S6, Supporting Information,

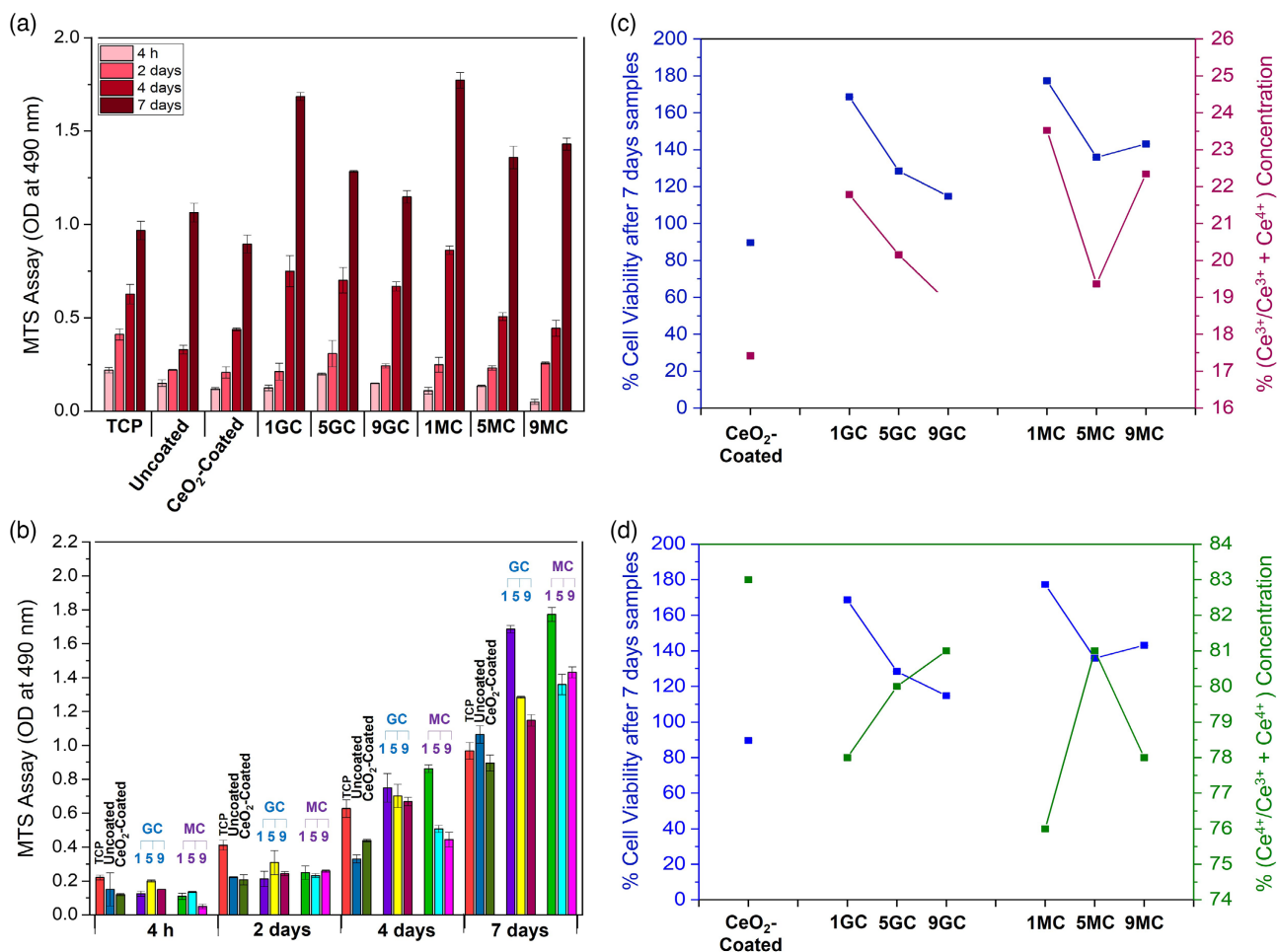


Figure 7. a,b) Cell attachment and proliferation of MG-63 cells cultured up to 7 days on: TCP, uncoated, CeO₂-coated, Ga-doped CeO₂-coated, and Mn-doped CeO₂-coated substrates analyzed by the MTS assay (OD at 490 nm), and c,d) effects of dopants on cytotoxicity values (for samples cultured for 7 days) and [Ce] from XPS data.

shows the peak-containing section of the GAXRD pattern. Although the indexing is uncertain, there appears to be α -quartz and HA, although these are represented by only single peaks. Three other peaks could not be assigned to any of the common phases that precipitate from silicate glasses,^[120] form by reaction between the bioglass and SBF,^[121] or precipitate from SBF.^[112,122–125] In the latter case, it has been established that the precipitation of HA from bioglass does not necessarily follow the stoichiometric Ca/P ratio of 1.67 for HA (Ca₁₀(PO₄)₆(OH)₂). Consequently, the approximately constant [P] is likely to have resulted from the establishment of interfacial chemical equilibrium between P released from the bioglass and its immediate incorporation in the adjacent HA, leaving the [P] of the surrounding SBF unchanged. As the [Ca] in the residual SBF decreased, this equilibrium would not apply to this ion and so the rate of deposition of Ca was greater than that of P transfer. It is probable that the commencement stage of deposition of Ca from the SBF initiated the transfer of P from the bioglass. The summary data in Figure 6f show that the Ca/P varied significantly between time points, which is consistent with the differential Ca deposition (fast) and P transfer (slow) rates.

2.8.2. CeO₂-Coated

The CeO₂-coated films showed more conventional behavior, where both the [Ce] and [P] decreased in response to the precipitation of HA. In this case, Figure 6f reveals that the Ca/P remained constant between time points, thus suggesting a single precipitation mechanism (from SBF), in contrast to the positive control. Comparison of these two sets of data is informative in that both show that, compared to the SBF composition, the Ca/P ratio in the residual SBF increased, meaning that it decreased in the HA. This comparison confirms that the deposition rate of Ca from SBF is greater than that of transfer of P from the bioglass but that the deposition rate of P from SBF is equivalent to that of Ca.

2.8.3. Ga-Doped (1GC, 5GC, 9GC)

Figure 7d,e shows that, compared to the CeO₂-coated films, the residual [Ca] after 2 weeks immersion was the same but that, after 1 month, the residual [Ca] decreased. At the same time, the residual [P] was higher after 2 weeks but it was approximately

unchanged after 1 month. However, Figure 6f shows that the Ca/P ratio remained approximate constant for 1GC, 5GC, and 9GC at both time points. These data reflect the different Ca/P ratios between the CeO₂-coated films and the Ga-doped films; they also show that the HA deposits from SBF in a consistent manner. Ultimately, it is apparent that Ga doping does not affect the Ca/P ratio.

2.8.4. Mn-Doped (1MC, 5MC, 9MC)

The data for the Mn-doped films are essentially the same as those for the Ga-doped samples, with the exception of 9MC after 2 weeks immersion. Here, the residual [Ca] was lower and the residual [P] was higher than those for the CeO₂-coated films. This probably resulted from the low amount of precipitated HA, as indicated in Figure S5h, Supporting Information. However, with even less HA precipitation after 1 month immersion, this difference is absent. Consequently, the reason for this differential is not clear.

For both the Ga-doped and Mn-doped films, the Ca/P ratios of the residual SBF were lower than those for the CeO₂-coated films, meaning that they were higher in the HA precipitates. Consequently, it is clear that both dopants effectively increased the Ca/P ratios in the HA films relative to those of the CeO₂-coated films. Although not overt in Figure 6f, there appears to be a slight decreasing Ca/P trend with increasing dopant level, thus further supporting this conclusion. The cause of this is unlikely to be the effect of dissolved Ga and Mn because Figure 7b,c reveals that the solubilities of the two ions are considerably different. It is possible that lattice distortion from the dopant dissolution alters the lattice parameters, thus cause lattice strain in the precipitated HA to be compensated by alteration of the Ca/P ratio. This has been shown to be the case elsewhere.^[126–128]

2.9. Cell Adhesion and Proliferation Assays

The results of cell adhesion and cell viability, which were assessed in vitro by the MTS assay, are shown in Figure 7; FESEM micrographs at the 4 h and 2 day time points are shown in Figure 8. The data in Figure 7 reveal the following.

2.9.1. Figure 7a

The numbers of cells increased for all of the samples up to 7 days. Of these, 1MC and 1GC reached the highest levels of cell numbers. The relative peak heights show that the dose dependence is the most significant factor and that the type of dopant is secondary. Although other studies confirm the priority of the dose dependence,^[63,91,129,130] there do not appear to be any other studies allowing comparison with the type of dopant. The probable reason for this is that Mn is a natural component of bone^[131] while this is not the case for Ga.

The CeO₂-coated sample exhibited much lower numbers of cells, even lower than those for TCP and the uncoated sample. Consequently, it is clear that CeO₂ is not favored by osteoblastic-like cells but that minor amounts of Ga and Mn alter this significantly.

The dose dependency is emphasized by the different trends for the increasing dopant levels, where Ga decreased regularly while Mn exhibited a minimum. Figure 2 reveals the great significance of [Ce³⁺] in that these two trends are duplicated.

The trend of cell numbers was descending for Ga-doped samples as a result of increasing the [Ga]. However, Mn revealed a little different trend, with the lowest cell numbers at 5 mol% and slightly increased at 9 mol%, which was still lower than that of for 1 mol%.

2.9.2. Figure 7b

4 h: At the shortest time point, there is little differentiation between samples, with the exception of the statistically significant difference ($p < 0.001$) between TCP and 9MC, where the latter supports the conclusion of the dose dependency of the growth and associated attachment delay for this biological cation. However, the similarity of the other data supports the view that there is a significant chemistry dependence.

2 Days: The cell growth increased only marginally at this time point, including 9MC. This is unusual in that it is normal for the cell growth to double at this time point.^[132] These data emphasize the primacy of the chemistry dependence at the shorter time points during the growth phase.

4 Days: There are several statistically significant differences: 1) The 1MC (highest) and uncoated (lowest) samples relative to TCP exhibited the greatest difference ($p < 0.0001$). 2) 1GC, 5GC, 9GC, and 1MC were extremely increasing relative to the uncoated and CeO₂-coated samples ($p < 0.0001$). 3) 5MC was very significantly increasing relative to the uncoated sample ($p < 0.01$). 4) The CeO₂-coated sample and 9MC also were very significantly decreasing relative to TCP ($p < 0.01$).

These data confirm that doping improved the cell proliferation over that of CeO₂. They also confirm the dose dependency of the cell proliferation, which was more significant Mn compared to Ga. This observation indicates that, even though Mn is intrinsic to bone, there is an overdoped point of diminishing returns.

7 Days: There are several statistically significant differences: 1) All of the doped samples were extremely increasing relative to TCP and the CeO₂-coated samples ($p < 0.0001$). 2) 1GC, 5GC, and all the Mn-doped samples were extremely increasing relative to the uncoated sample ($p < 0.0001$). 3) The CeO₂-coated sample was very significantly decreasing relative to the uncoated sample ($p < 0.01$).

All but one of the samples, even the uncoated sample, revealed improvements in cell proliferation. The single exception was the CeO₂-coated sample. Although this showed the least cell proliferation, the OD still increased fivefold over that at 4 h. These data highlight the primary of the dose dependency on cell proliferation rather than the chemistry (which better reflects the cell growth).

2.9.3. Figure 7c

All of the samples exhibited cell viabilities >86%, which are significantly greater than the commonly accepted benchmark of 70% (EN ISO 10993-5: 2009) for acceptable cell viability.^[133–135]

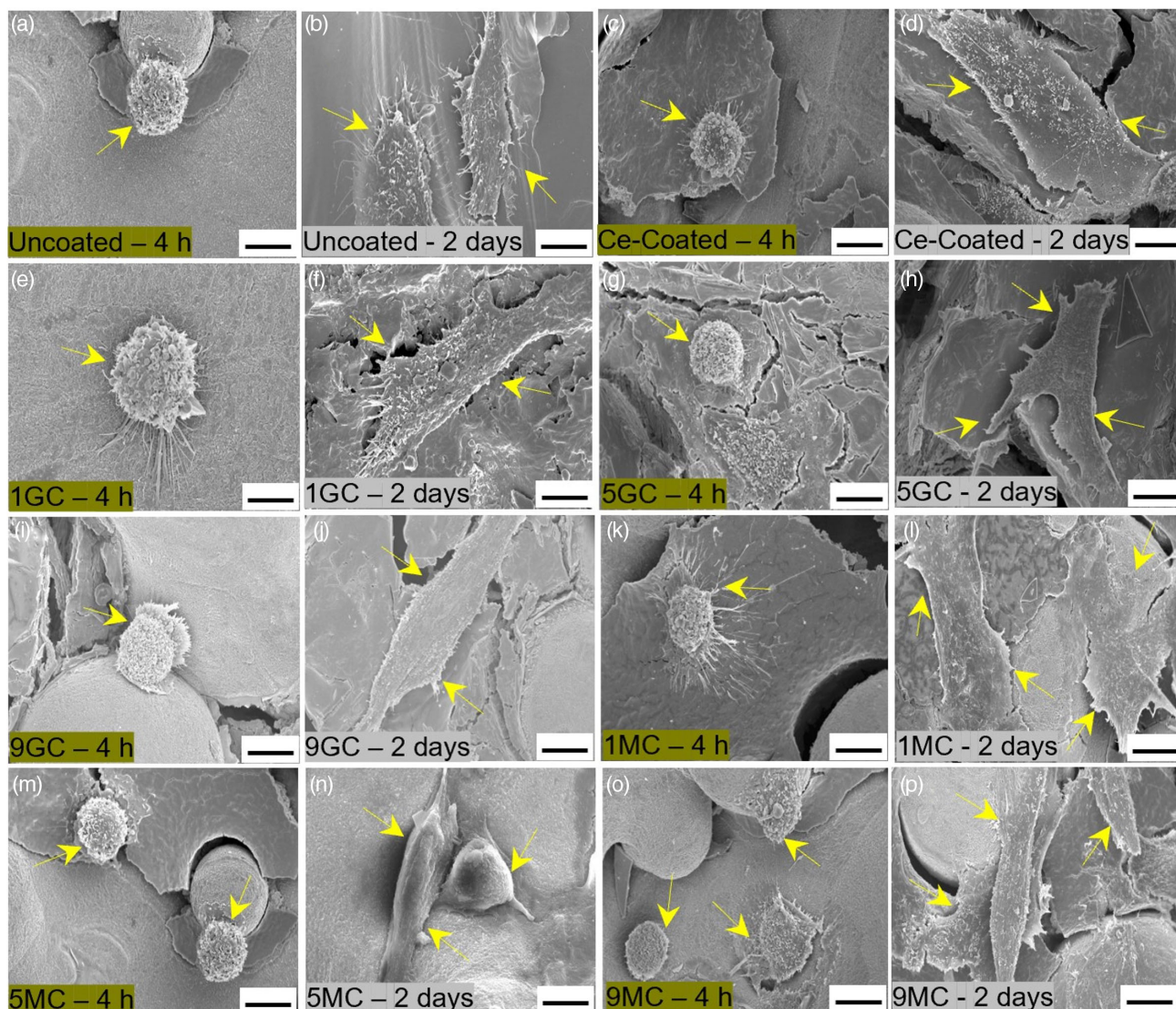


Figure 8. FESEM images of cell attachment (4 h) and cell proliferation (2 days) following seeding by MG-63 cells on the substrates for: a,b) uncoated, c,d) CeO₂-coated, e–j) Ga-doped CeO₂-coated, and k–p) Ga-doped CeO₂-coated substrates (5 μm scale bar).

The data for [Ce³⁺] in Figure 2 are repeated here and contrasted with those for cell viability after 7 days. The close parallels are clearly apparent, where both (specific) chemistry dependence and dose dependence are clear.

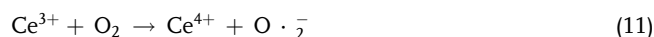
The chemistry dependence is revealed by the slightly superior performance of the Mn-doped samples. The dose dependence is revealed by the initial increase (from undoped) and the subsequent decreases with increasing dopant concentration.

The overall dependency on the [Ce³⁺] is revealed by the parallels in the data for cell viability.

2.9.4. Figure 7d

These data for [Ce⁴⁺] show converse trends of those of [Ce³⁺] for the reason that these data are normalized to 100% from the respective XPS peak areas.

These data are presented in order to emphasize the role of ROS generation in reducing the cell viability, as exemplified by, for example



It is common practice to attribute these effects to the role of V_O[•] and to equate the [V_O[•]] with one half the [Ce³⁺].^[69,136] Further, it is implicit that these interpretations assume substitutional solid solubility and ionic charge compensation. However, the present work demonstrates that ionic charge compensation is not the case and that redox charge compensation from substitutional solid solubility and IVCT (with perhaps a small influence from electronegativity) are. Therefore, the addition of acceptor dopants, such as Mn²⁺, Mn³⁺, and Ga³⁺, cannot generate oxygen vacancies. Instead, they generate Ce³⁺, which can be determined

directly by XPS. The data in Figure 7c confirm the critical importance of Ce^{3+} as it provides a direct reflection of its dominant influence on the cell viability, where this ion is beneficial.

The images in Figure 8a–p reveal that all the substrates supported the initial cellular attachment after 4 h, followed by cellular extension and continuous growth during the following 2 days. After 2 days, the cells had become interconnected, as indicated by the elongated lamellipodia, which are common features of MG-63 cells.^[137]

2.9.5. Importance of $Ce^{4+} \leftrightarrow Ce^{3+}$ Redox

The cytoprotective capacity of ceria derives mainly from the continuously reversible $Ce^{4+} \leftrightarrow Ce^{3+}$ redox switching, which regulates the ROS level.^[138] That is, ceria acts as an antioxidant by scavenging the ROS at basic physiological pH, thereby protecting normal cells, while ceria acts as a prooxidant by generating ROS at acidic tumor microenvironment (TME) pH, thereby killing cancerous cells.^[139,140] A critical consideration is valence implications of this redox switching,^[138] where it is known that the $[Ce^{3+}]$ is higher in basic physiological pH while $[Ce^{4+}]$ is higher in acidic TME.^[141]

2.10. Summary and Conclusions

2.10.1. Summary

For the porous films of ceria doped with 1, 5, or 9 mol% Ga or Mn, spin coated on rough Ti6Al4V substrates, **Table 4** contrasts the combinations of factors that affect the bacterial survival and cell viabilities.

With increasing [Ga], the increasing viscosity led to greater continuity of the film as coating; with increasing [Mn], a reverse but reduced effect was observed, so the substrate asperities remained discrete projections above all of the films. Consequently, the dopant concentrations to which the bacteria and cells were exposed were a function of the dopant concentration (from doping), the area of exposed film surrounding the projecting asperities (from viscosity), and oxide precipitation (from precipitation). For Ga doping, the first two trends were in parallel

(precipitation was absent) but, for Mn doping, the increasing trends from doping and precipitation did not match the constancy of film exposure from the lower viscosity compared to the increasing viscosity trend for Ga doping.

The final variables examined were surface and subsurface $[Ce^{3+}]$. For Ga doping, the trend for the surface $[Ce^{3+}]$ was the reverse of that expected from the dopant concentration, indicating that this parameter is controlled by Ce redox and IVCT (Equation (3)). For Mn doping, the trend revealed a minimum in $[Ce^{3+}]$, suggesting differential effects, which result from overdoping and the introduction of a second solubility mechanism. Further contributions could derive from IVCT between film and substrate (Equation (4–6)) and/or surface broken bonds versus lattice bonds. For both Ga doping and Mn doping, the subsurface $[Ce^{3+}]$ reflects the competition between surface broken bonds versus lattice bonds and the interaction between the film and substrate.

2.10.2. Bacterial Survival

All of the films exhibited superior bactericidal activity against *S. aureus* (gram-positive) compared to that against *E. coli* (gram-negative). As stated, this suggests that the surface charge of all of the films is negative, which indicates the dominant effect on the bacteria of Ce^{3+} over that of Ce^{4+} , despite the fact that $[Ce^{4+}] > [Ce^{3+}]$ (Figure 2 and Table S4, Supporting Information). Further, the bactericidal activity of Mn generally was superior to that of Ga.

The bacterial survival percentages depend on the combined effects of the variables roughness, $[Ce^{3+}]$, Ti alloy surface charge from the asperities, and dopant concentration. For the homogeneous solid solutions 1GC and 5GC, the effects of both roughness and Ti alloy surface charge dominated while 9GC was dominated by the low $[Ce^{3+}]$ owing to the greater coverage of the Ti alloy substrate. For the inhomogeneous Mn-doped samples and gram-positive *S. aureus*, the dominant effects of roughness and negatively charged Mn_3O_4 were apparent. For gram-negative *E. coli*, the only notable effect was that of the low roughness and low $[Ce^{3+}]$ for 9MC.

Table 4. Summative comparison of data.

Sample Parameter	CeO ₂ -coated	Ga-doped			Mn-doped		
		1GC	5GC	9GC	1Mn	5Mn	9Mn
Bacterial survival (gram +) [%]	6.4	4.9	4.2	8.5	5.4	0.8	0.9
Bacterial survival (gram –) [%]	9.2	9.6	9.2	5.2	6.8	7.5	7.5
Mammalian cell viability [%]	90	169	129	115	177	136	143
Wettability	High	High	Medium	Low	High	High	High
R _s roughness [μm]	14	17	13	5	25	12	11
[Dopant] from doping [mol%]	0	1	5	9	1	5	9
[Dopant] from precipitation	–	Nil	Nil	Nil	Low	Medium	High
[Dopant] from viscosity	–	Low	Medium	High	Low	Low	Low
Surface $[Ce^{3+}]$ [at%]	17	22	20	19	24	19	22
Subsurface $[Ce^{3+}]$ [at%]	26	26	13	14	31	17	24

2.10.3. Acellular Mineralization

The results for HA formation was distinctive, yielding Ca/P ratios in the general range ≈ 1.6 – 2.1 . Following soaking in SBF for 2 weeks or 1 month, no HA formation on the CeO₂-coated samples was observed. In contrast, the presence of the homogeneous Ga-doped CeO₂ solid solution enhanced HA formation considerably, where it was clear that the [Ga] was proportional to the extent of HA formation. In contrast, the Mn-doped samples showed the reverse trend. These differences are attributed to the role of [Ce³⁺], where the extent of HA formation on the homogeneous Ga-doped solid solutions is inversely proportional to the [Ce³⁺], which may act as a nucleation site. This effect was reversed for the inhomogeneous Mn-doped samples.

2.10.4. Mammalian Cell Viability

The direct relation between cell attachment and proliferation and the [Ce³⁺] was overt, where both undoped and doped samples exhibited direct correlations between these factors. Further, the bioactivity increased in the order CeO₂-coated < Ga-doped < Mn-doped. The interpretation of these data is distinctive in light of the fact that the defect equilibria indicate the absence of a role for oxygen vacancies. As stated previously, essentially all of the reports of the effects of Ce redox on cell interactions attribute the resultant effects to oxygen vacancies, the formation of which is assumed to result from Ce⁴⁺ → Ce³⁺ reduction and charge compensation. In the present work, this assumption has been shown to be unjustified, leading to the conclusion that the dominant effect derives of the surface [Ce³⁺].

3. Conclusions

The present work highlights a number of conclusions that can be made on the basis of the data analysis. First, the solubility mechanisms of Ga and Mn in CeO₂ have been considered. Second, the simultaneous examination of these two dopants, as opposed to the more typical examination of a single dopant, allows the decoupling of many of the phenomena. Third, data analysis that combines XPS data with defect equilibria is shown to be a powerful tool to determine solid solubility mechanisms, charge compensation mechanisms, the formation of different defect types, and their roles in the performance of materials. Fourth, anomalous data (5MC vs 9MC) elucidate the potential for a change in solubility mechanism and resultant charge compensation mechanisms as a function of dopant level. Fifth, the bacterial survival percentages, acellular mineralization, and cell viability are strongly dependent on the [Ce³⁺], not the [V_O[•]]. Sixth, cytotoxicity derives from formation of ROS, which results from Ce³⁺ → Ce⁴⁺.

4. Experimental Section

Preparation of Doped-CeO₂ Thin Films: The substrates used were 3D-printed biomedical-grade titanium-alloy sheets Ti6AlV4 (1 × 1 × 0.1 cm³, Advanced Manufacturing Services, Australia) with an R_a roughness of $\approx 16 \pm 0.2$ μm. These characteristics suggest the potential for good coating/substrate bond strength owing to the interlocking and facilitation of cell adhesive owing to the presence of asperities. Prior to coating, each

substrate was cleaned ultrasonically for 1 h sequentially in acetone and ethanol, followed by rapid drying in flowing N₂. The precursor solution for the CeO₂ thin films was prepared by dissolving cerium nitrate hexahydrate (Ce(NO₃)₃·6H₂O, 99.99 wt% trace metal basis, Sigma-Aldrich, Australia) in isopropanol (Reagent Plus, 99 wt%, Sigma-Aldrich, Australia) to obtain 1 M concentration (43.422 g of Ce(NO₃)₃·6H₂O was dissolved in 100 mL of isopropanol) by magnetic stirring for 2 h in a Pyrex beaker. Dopant salts Mn(NO₃)₂·4H₂O (98 wt%, Sigma-Aldrich) and Ga(NO₃)₃·9H₂O (99.9 wt%, Sigma-Aldrich, Australia) were used at the concentrations 0.00, 1.00, 5.00, and 9.00 mol% (metal basis). Each solution was stirred magnetically for 2 h in a Pyrex beaker. Although the system was nonaqueous, the pH (Laquatwin, Horiba Scientific, Japan) was measured to be in the range ≈ 1.2 – 1.6 . Spin coating (Laurell Technologies, WS-65052, USA) was carried out by deposition of 0.2 mL (\approx ten drops) of each solution onto a substrate while spinning at 2000 rpm, followed by drying by spinning for ≈ 10 s and then placing on a hot plate at preheated to 50 °C for 15 min. These processes were repeated nine additional times for a total of ten coatings, which resulted in the fabrication of continuous coatings without macroscopic crack formation. Following these procedures, all of the samples were placed simultaneously on a high-Al₂O₃ firebrick and calcined in a muffle furnace at 650 °C for 2 h (heating rate of 1 °C min⁻¹; natural cooling).

Material Characterization: The samples were either platinum coated (with fixed cells; Leica EM ACE600 Sputter Coater, Leica Microsystems, Germany, 10 kPa) or carbon coated (without fixed cells; K575X Sputter Coater, UK). Cross sections of the nanostructures were analyzed by focused ion beam (FIB; FEI xT Nova NanoLab 200 FIB/SEM, USA, 300 kV) and the surface nanostructures were examined by FESEM (FEI Nova NanoSEM 450, USA, 15 kV, 50 kV, secondary electron imaging mode). The surface topographies were analyzed using 3D scanning laser confocal microscopy (VK-X260K, USA, violet laser, 408 nm) at 20× magnification. The mineralogy of the ceria samples was determined by GAXRD (PANalytical Empyrean Thin Film XRD, UK, 45 kV, 40 mA, 1° angle of incidence (0.033° s⁻¹ 2θ step speed, 0.026° 2θ step size, 0°–100° 2θ range). No peaks at angles lower than 20° 2θ were detected. The surface chemistries and ion valences were analyzed by XPS (ESCALAB 250Xi X-ray photoelectron spectrometer microprobe, Thermo Fisher Scientific, UK, 13 kV, 12 mA, 500 μm spot size). The ionic concentrations of the Ce, Ga, Mn, Ca, and PO₄ after immersion in the SBF solution were determined by inductively coupled plasma optical emission spectroscopy (ICP-OES, PerkinElmer Optima, USA). The viscosities of the sol–gel precursors were assessed by placing a drop of precursor on a fully dense Ti6Al4V substrate (Sunray Oil Equipment Pty. Ltd., Singapore supplier), followed by photographing ≈ 10 s later.

Bacterial Culture: *S. aureus* strain 38 and *E. coli* strain K12 were grown separately on nutrient agar (OXOID, UK) by incubating at 37 °C for 18 h. Multiple colonies then were transferred to 10 mL tryptone soy broth medium (TSB; OXOID, UK) and incubated for 24 h. The bacteria were collected by centrifugation (5000 g for 10 min), washed two times with 1 M phosphate-buffered saline (PBS; Thermo Fisher Scientific, UK), and pipetted into 40 mL of fresh TSB. The optical density (OD) was adjusted to 0.1 660 nm in TSB, which is equivalent to 10⁸ colony forming units per mL of suspension (CFU mL⁻¹). All substrates and ceria samples were autoclaved, rinsed with ethanol, and washed thoroughly with 1 M PBS. SEM examination revealed no alteration of either the substrates or the films from autoclaving. Following this, 4 mL of *S. aureus* or *E. coli* was pipetted into each well of a 6-well plate containing the ceria and orbitally shaken (120 rpm) for 24 h at 37 °C. The media were removed and each well was rinsed twice with PBS to remove nonadherent bacteria. Each sample was placed in a sterile lidded plastic tube containing 2 mL of PBS, sealed, stirred with a magnetic stirring bar for 2 min, and vortexed vigorously for 2 min in order to release the adhered bacteria from the surfaces. Triplicate aliquots of the serial dilutions were cultured on nutrient agar and incubated for 24 h at 37 °C, after which the numbers of CFU were determined. These experiments were performed twice in triplicate, using uncoated samples as negative controls. Statistical evaluation on the comparisons between coated and uncoated samples was done by one-way analysis of variance (ANOVA) followed by Tukey's multiple-comparison

test. The statistical significance (*p*-values) was calculated using Prism 8 Software.

Acellular Mineralization: SBF containing NaCl, NaHCO₃, KCl, K₂HP₄·3H₂O, MgCl₂·6H₂O, CaCl₂, Na₂SO₄, Tris, and 1 M HCl (pH 7.4) was prepared according to the Kokubo method.^[142] The ionic concentrations of the SBF compared with those of human blood plasma are given in Table S3, Supporting Information. The samples were sterilized by autoclaving, dip-cleaned in ethanol, washed in triplicate by spray (pipette) washing with 1 M PBS, and immersed in SBF solution. CeO₂, Ga-doped CeO₂, and Mn-doped CeO₂ coatings as well as a powdered, resorbable, bioactive, glass material (Bioactive Bone Graft, 200–400 μm Unigraft, USA; containing Ca, P, and Si; as positive control) were placed in individual polypropylene containers containing 150 mL SBF solution. Each container was incubated at 37 °C and samples removed after 2 weeks (15 d) or 1 month (30 d). Each solution of residual SBF was analyzed by ICP-OES (PerkinElmer Optima, USA). These tests were done independently, not contiguously. Analyses for the concentrations of Ce, Ga, and Mn were done as single measurements but those for Ca and P were done in triplicate. The samples subsequently were examined by FESEM and GAXRD.

Cell Culture: Human osteoblast-like cells (MG-63; ATCC CRL-1427TM) were used as they have functional characteristics similar to those of pre-osteoblastic cells and they have been shown to serve as a successful model for the study of cell adhesion, proliferation, and differentiation.^[143–146] MG-63 cells were cultured in Dulbecco's Modified Eagle Medium (DMEM; Sigma-Aldrich, Australia) supplemented with 1 mM sodium pyruvate, 4 mM L-glutamine, 100 mg L⁻¹ streptomycin, 10% v/v fetal bovine serum, and 1% v/v nonessential amino acids.^[147] The samples were sterilized by autoclaving, dip-cleaning in ethanol, and washing in triplicate by spray (pipette) washing with 1 M PBS. The cells were seeded at 2 × 10⁴ cells/well into each well of a 24-well polystyrene plate (Ultra-Low Attachment 24-Well Plate, Corning Inc., USA) that contained either sample (uncoated ceria, CeO₂, Ga-doped CeO₂, or Mn-doped CeO₂ ceria), or no sample. Of the latter, positive controls (treated culture plate [TCP]) were wells containing cells and media only while negative controls were wells with media alone. The cell culturing was performed in triplicate and samples analyzed after 4 h, 2, 4, and 7 d.

The plates were incubated in a humidified atmosphere (95% RH) at 37 °C and 5% CO₂. Cell adhesion and proliferation were examined by the MTS assay (MTS assay, Promega, Australia) according to the manufacturer's instructions. The MTS reagent, tetrazolium inner salt 3-(4,5-dimethylthiazol-2-yl)-5-(3-carboxymethoxyphenyl)-2-(4-sulfophenyl)-2H-tetrazolium, was added to all wells 4 h prior to each abovenamed time point, followed by 4 h further incubation (the exception was for the first time point, when MTS was added at 3.5 h, followed by incubation for 30 min). Subsequently, 100 μL from each well was pipetted and transferred to a 96-well polystyrene plate (Sigma-Aldrich) and analyzed immediately by UV–vis absorbance spectrophotometry at 490 nm using a plate reader (SynergyTM HTX Multi-Mode Microplate Reader, BioTek Instruments, USA).

For analysis by electron microscopy, samples with attached cells were removed from the wells and placed in the wells of a new 24-well polystyrene plate (Corning Inc., USA). Any dead cells were removed by washing in 1 mL of 0.1 M PBS after which cells were fixed in 2.5% v/v glutaraldehyde, followed by curing in air at 20 °C for 30 min. The fixative was removed from each well and the samples were washed three times by soaking for 5 min in 0.1 M PBS. The samples then were dehydrated by soaking in a series of aqueous ethanol solutions of increasing concentration (30%, 50%, 70%, 90%, and 100%) for 30 min each, with the final soak being performed twice. After removal of the ethanol, 0.5 mL of bis(trimethylsilyl)amine (HMDS, Sigma-Aldrich) was added to each well and the plate was cured in air at 20 °C for 20 min. Following removal of the HMDS, the plate was dried in air at 20 °C for 12 h.

Supporting Information

Supporting Information is available from the Wiley Online Library or from the author.

Acknowledgements

The authors acknowledge the financial support of the Australian Research Council (ARC) (DP170104130), the UPA Scholarship from UNSW Sydney, Australia. The authors thank Dr. Yin Yao for technical assistance and use of facilities at the Electron Microscope Unit within the Mark Wainwright Analytical Centre at UNSW Sydney.

Conflict of Interest

The authors declare no conflict of interest.

Data Availability Statement

The data that support the findings of this study are available from the corresponding author upon reasonable request.

Keywords

antibacterial, Ce³⁺, ceria, cytotoxicity, solid solubility

Received: January 16, 2022

Revised: April 22, 2022

Published online:

- [1] A. S. R. Steven, M. Kurtz, in *73 rd annual meeting of the American Academy of Orthopaedic Surgery* **2006**, <https://www.webmd.com/osteoarthritis/news/20060324/joint-replacement-surgery-on-rise>.
- [2] *Australian Orthopaedic Association National Joint Registry - 20th Annual Report 2019, 2019*.
- [3] S. Kurtz, K. Ong, E. Lau, F. Mowat, M. Halpern, *J. Bone Joint Surg.* **2007**, *89*, 780.
- [4] J. Raphael, M. Holodniy, S. B. Goodman, S. C. Heilshorn, *Biomaterials* **2016**, *84*, 301.
- [5] J. Morris, N. Kelly, L. Elliott, A. Grant, M. Wilkinson, K. Hazratwala, P. McEwen, *Surg. Infect.* **2019**, *20*, 16.
- [6] B. Li, T. J. Webster, *J. Orthop. Res.* **2018**, *36*, 22.
- [7] T. Albrektsson, W. Becker, P. Coli, T. Jemt, J. Molne, L. Sennerby, *Clin. Implant. Dent. Relat. Res.* **2019**, *21*, 786.
- [8] C. E. Heim, D. Vidlak, T. D. Scherr, C. W. Hartman, K. L. Garvin, T. Kielian, *J. Immunol.* **2015**, *194*, 3861.
- [9] L. Cremet, A. Broquet, B. Brulin, C. Jacqueline, S. Dauvergne, R. Brion, K. Asehnoune, S. Corvec, D. Heymann, N. Caroff, *Pathog. Dis.* **2015**, *73* fiv065.
- [10] M. Ribeiro, F. J. Monteiro, M. P. Ferraz, *Biomater* **2012**, *2*, 176.
- [11] C. R. Arciola, D. Campoccia, L. Montanaro, *Nat. Rev. Microbiol.* **2018**, *16*, 397.
- [12] H. Chouirfa, H. Bouloussa, V. Mignonney, C. Falentin-Daudre, *Acta Biomater.* **2019**, *83*, 37.
- [13] E. M. Greenfield, Y. Bi, A. A. Ragab, V. M. Goldberg, J. L. Nalepka, J. M. Seabold, *J. Biomed. Mater. Res.* **2005**, *72B* 179.
- [14] M. Prakasam, J. Locs, K. Salma-Ancane, D. Loca, A. Largeteau, L. Berzina-Cimdina, *J. Funct. Biomater.* **2017**, *8*, 1.
- [15] M. Kaur, K. Singh, *Mater. Sci. Eng., C* **2019**, *102*, 844.
- [16] M. Navarro, A. Michiardi, O. Castano, J. A. Planell, *J. R. Soc. Interface* **2008**, *5*, 1137.
- [17] C. C. Wang, Y. C. Hsu, F. C. Su, S. C. Lu, T. M. Lee, *J. Biomed. Mater. Res. A* **2009**, *88*, 370.
- [18] E. Matykina, J. M. Hernandez-López, A. Conde, C. Domingo, J. J. de Damborenea, M. A. Arenas, *Electrochim. Acta* **2011**, *56*, 2221.

- [19] J. Jiang, G. Han, X. Zheng, G. Chen, P. Zhu, *Surf. Coat. Technol.* **2019**, 375, 645.
- [20] Z. Xia, X. Yu, X. Jiang, H. D. Brody, D. W. Rowe, M. Wei, *Acta Biomater* **2013**, 9, 7308.
- [21] L. Esteban-Tejeda, L. A. Díaz, B. Cabal, C. Prado, R. López-Piriz, R. Torrecillas, J. S. Moya, *Mater. Lett.* **2013**, 111, 59.
- [22] L. Mai, D. Wang, S. Zhang, Y. Xie, C. Huang, Z. Zhang, *Appl. Surf. Sci.* **2010**, 257, 974.
- [23] A. Cochis, B. Azzimonti, R. Chiesa, L. Rimondini, M. Gasik, *ACS Biomater. Sci. Eng.* **2019**, 5, 2815.
- [24] I. Braceras, M. A. Pacha-Olivenza, A. Calzado-Martín, M. Multigner, C. Vera, L. L. Broncano, A. M. Gallardo-Moreno, J. L. González-Carrasco, N. Vilaboa, M. L. González-Martín, *Appl. Surf. Sci.* **2014**, 310, 36.
- [25] I. C. Saldarriaga Fernandez, H. C. Mei, S. Metzger, D. W. Grainger, A. F. Engelsman, M. R. Nejadnik, H. J. Busscher, *Acta Biomater.* **2010**, 6, 1119.
- [26] Z. Xu, M. Li, X. Li, X. Liu, F. Ma, S. Wu, K. W. Yeung, Y. Han, P. K. Chu, *ACS Appl. Mater. Interfaces* **2016**, 8, 16584.
- [27] K. Huo, X. Zhang, H. Wang, L. Zhao, X. Liu, P. K. Chu, *Biomaterials* **2013**, 34, 3467.
- [28] J. Ye, J. Deng, Y. Chen, T. Yang, Y. Zhu, C. Wu, T. Wu, J. Jia, X. Cheng, X. Wang, *Biomater. Sci.* **2019**, 7, 2826.
- [29] R. A. Surmenev, M. A. Surmeneva, A. A. Ivanova, *Acta Biomater* **2014**, 10, 557.
- [30] T. Crouzier, K. Ren, C. Nicolas, C. Roy, C. Picart, *Small* **2009**, 5, 598.
- [31] A. L. Rosa, M. M. Beloti, R. van Noort, *Dent. Mater.* **2003**, 19, 768.
- [32] Y.-F. Goh, A. Z. Alshemary, M. Akram, M. R. Abdul Kadir, R. Hussain, *Ceram. Int.* **2014**, 40, 729.
- [33] H. Li, P. Xia, S. Pan, Z. Qi, C. Fu, Z. Yu, W. Kong, Y. Chang, K. Wang, D. Wu, X. Yang, *Int. J. Nanomed.* **2020**, 15, 7199.
- [34] C. L. Santos, A. J. R. Albuquerque, F. C. Sampaio, D. Keyson, *Nanomaterials with Antimicrobial Properties: Applications in Health Sciences*, **2013**.
- [35] D. M. Aruguete, B. Kim, M. F. Hochella, Y. Ma, Y. Cheng, A. Hoegh, J. Liu, A. Pruden, *Environ. Sci. Processes Impacts* **2013**, 15, 93.
- [36] D. A. Pelletier, A. K. Suresh, G. A. Holton, C. K. McKeown, W. Wang, B. Gu, N. P. Mortensen, D. P. Allison, D. C. Joy, M. R. Allison, S. D. Brown, T. J. Phelps, M. J. Doktycz, *Appl. Environ. Microbiol.* **2010**, 76, 7981.
- [37] X. Li, M. Qi, X. Sun, M. D. Weir, F. R. Tay, T. W. Oates, B. Dong, Y. Zhou, L. Wang, H. H. K. Xu, *Acta Biomater.* **2019**, 94, 627.
- [38] O. I. Zeyons, A. Thill, F. Chauvat, N. Menguy, C. Cassier-Chauvat, C. d. OrTar, J. Daraspe, M. I. Auffan, J. r. Rose, O. Spalla, *Nanotoxicology* **2009**, 3, 284.
- [39] Y. Liu, B. Rath, M. Tingart, J. Eschweiler, *J. Biomed. Mater. Res. A* **2020**, 108, 470.
- [40] N. Harrison, P. E. McHugh, W. Curtin, P. Mc Donnell, *J. Mech. Behav. Biomed. Mater.* **2013**, 21, 37.
- [41] R. Z. LeGeros, *Clin. Orthop. Relat. Res.* **2002**, 395, 81.
- [42] J. R. Jones, *Acta Biomater.* **2013**, 9, 4457.
- [43] V. Sollazzo, F. Pezzetti, A. Scarano, A. Piattelli, C. A. Bignozzi, L. Massari, G. Brunelli, F. Carinci, *Dent. Mater.* **2008**, 24, 357.
- [44] P. C. Bessa, M. Casal, R. L. Reis, *J. Tissue Eng. Regen. Med.* **2008**, 2, 81.
- [45] D. S. Brauer, *Angew. Chem., Int. Ed.* **2015**, 54, 4160.
- [46] M. Yamaguchi, *Mol. Cell. Biochem.* **2010**, 338, 241.
- [47] P. M. Torres, S. I. Vieira, A. R. Cerqueira, S. Pina, O. A. da Cruz Silva, J. C. Abrantes, J. M. Ferreira, *J. Inorg. Biochem.* **2014**, 136, 57.
- [48] A. Balamurugan, G. Balossier, D. Laurent-Maquin, S. Pina, A. H. Rebelo, J. Faure, J. M. Ferreira, *Dent. Mater.* **2008**, 24, 1343.
- [49] V. Mouriño, P. Newby, A. R. Boccaccini, *Adv. Eng. Mater.* **2010**, 12 B283.
- [50] D. Schubert, R. Dargusch, J. Raitano, S. W. Chan, *Biochem. Biophys. Res. Commun.* **2006**, 342, 86.
- [51] M. Horie, K. Nishio, H. Kato, K. Fujita, S. Endoh, A. Nakamura, A. Miyauchi, S. Kinugasa, K. Yamamoto, E. Niki, Y. Yoshida, Y. Hagihara, H. Iwahashi, *J. Biochem.* **2011**, 150, 461.
- [52] J. D. Cao, N. T. Kirkland, K. J. Laws, N. Biribilis, M. Ferry, *Acta Biomater.* **2012**, 8, 2375.
- [53] N. Eliaz, N. Metoki, *Materials* **2017**, 10, 334.
- [54] S. Vogt, K. D. Kühn, U. Gopp, M. Schnabelrauch, *Materialwiss. Werkstofftech* **2005**, 36, 814.
- [55] K. Hareesh, A. V. Deore, S. S. Dahiwal, G. Sanjeev, D. Kanjilal, S. Ojha, N. A. Dhole, K. M. Kodam, V. N. Bhoraskar, S. D. Dhole, *Radiat. Phys. Chem.* **2015**, 112, 97.
- [56] X. Li, J. Qiu, X. Liu, *Adv. Mater. Interfaces* **2020**, 7, 14922.
- [57] J. Narasimhan, C. R. Chltambar, *Pathobiology* **1991**, 59, 3.
- [58] R. D. Shannon, C. T. Prewitt, *Acta Crystallogr. Sec. B* **1969**, 25, 925.
- [59] N. Gómez-Cerezo, E. Verron, V. Montouillout, F. Fayon, P. Lagadec, J. M. Boulter, B. Bujoli, D. Arcos, M. Vallet-Regí, *Acta Biomater.* **2018**, 76, 333.
- [60] R. P. Warrell, B. Bosco, S. Weinerman, B. Levine, J. Lane, R. S. Bockman, *Ann. Intern. Med.* **1990**, 113, 847.
- [61] A. Mesaros, B. S. Vasile, D. Toloman, O. L. Pop, T. Marinca, M. Unguresan, I. Perhaita, M. Filip, F. Iordache, *Appl. Surf. Sci.* **2019**, 471, 960.
- [62] F. Lüthen, U. Bulnheim, P. D. Müller, J. Rychly, H. Jesswein, J. G. B. Nebe, *Biomol. Eng.* **2007**, 24, 531.
- [63] Y.-J. Bae, M.-H. Kim, *Biol. Trace Elem. Res.* **2008**, 124, 28.
- [64] A. B. Santamaria, S. I. Sulsky, *J. Toxicol. Environ. Health, Part A* **2010**, 73, 128.
- [65] A. Khosravanihaghighi, P. Koshy, G. Bahmanrokh, C. C. Sorrell, *Mater. Chem. Phys.* **2022**, 277, 125483.
- [66] R. Mehmood, S. S. Mofarah, W. F. Chen, P. Koshy, C. C. Sorrell, Subsurface Surface, *Inorg. Chem.* **2019**, 58, 6016.
- [67] D. R. Baer, K. Artyushkova, C. R. Brundle, J. E. Castle, M. H. Engelhard, K. J. Gaskell, J. T. Grant, R. T. Haasch, M. R. Linford, C. J. Powell, A. G. Shard, P. M. A. Sherwood, V. S. Smentkowski, *J. Vac. Sci. Technol., A* **2019**, 37, 031401.
- [68] M. Bagheri, P. Blaha, *J. Electron Spectrosc. Relat. Phenom.* **2019**, 230, 1.
- [69] G. Bahmanrokh, C. Cazorla, S. S. Mofarah, R. Shahmiri, Y. Yao, I. Ismail, W.-F. Chen, P. Koshy, C. C. Sorrell, *Nanoscale* **2020**, 12, 4916.
- [70] Y. Xu, S. S. Mofarah, R. Mehmood, C. Cazorla, P. Koshy, C. C. Sorrell, *Mater. Horiz.* **2020**.
- [71] V. Kumar, W.-F. Chen, X. Zhang, Y. Jiang, P. Koshy, C. C. Sorrell, *Ceram. Int.* **2019**, 45, 22085.
- [72] S. Yamaguchi, S. Nath, Y. Sugawara, K. Divakarla, T. Das, J. Manos, W. Chrzanowski, T. Matsushita, T. Kokubo, *Nanomaterials* **2017**, 7, 1.
- [73] C. H. Goss, Y. Kaneko, L. Khuu, G. D. Anderson, S. Ravishankar, M. L. Aitken, N. Lechtzin, G. Zhou, D. M. Czyn, K. McLean, O. Olakanmi, H. A. Shuman, M. Teresi, E. Wilhelm, E. Caldwell, S. J. Salipante, D. B. Hornick, R. J. Siehnell, L. Becker, B. E. Britigan, P. K. Singh, *Sci. Transl. Med.* **2018**, 10 eaat7520.
- [74] Z.-K. Han, L. Zhang, M. Liu, M. V. Ganduglia-Pirovano, Y. Gao, *Front. Chem.* **2019**, 7.
- [75] R. K. Foreman, M. Segura-Noguera, D. M. Karl, *Mar. Chem.* **2016**, 186, 83.
- [76] Y. Jiang, W.-F. Chen, P. Koshy, C. C. Sorrell, *J. Mater. Sci.* **2019**, 54, 5266.
- [77] F. A. Kröger, H. J. Vink, *Relations Between the Concentrations of Imperfections in Crystalline Solids* (Eds: F. Seitz, D. Turnbull), Solid State Physics, Academic Press, New York **1956**, pp. 307–435.
- [78] D. W. Smith, *J. Chem. Educ.* **1990**, 67, 911.
- [79] S. U. Awan, S. K. Hasanain, M. F. Bertino, G. H. Jaffari, *J. Appl. Phys.* **2012**, 112, 103924.

- [80] C. Chawengkijwanich, Y. Hayata, *Int. J. Food Microbiol.* **2008**, *123*, 288.
- [81] L. M. Bjursten, L. Rasmusson, S. Oh, G. C. Smith, K. S. Brammer, S. Jin, *J. Biomed. Mater. Res. A* **2010**, *92*, 1218.
- [82] L. K. Randeniya, A. Bendavid, P. J. Martin, M. S. Amin, R. Rohanizadeh, F. Tang, J. M. Cairney, *Diamond Relat. Mater.* **2010**, *19*, 329.
- [83] J. Gamage, Z. Zhang, *Int. J. Photoenergy* **2010**, *2010*, 1.
- [84] T. Kawano, W. Prananingrum, Y. Ishida, T. Goto, Y. Naito, M. Watanabe, Y. Tomotake, T. Ichikawa, *PLoS One* **2013**, *8*, e84327.
- [85] D. Shao, K. Li, M. You, S. Liu, T. Hu, L. Huang, Y. Xie, X. Zheng, *Appl. Surf. Sci.* **2020**, *504*, 343.
- [86] N. I. Aminuddin, R. Ahmad, H. M. Ansari, N. Mohd. Zain, S. A. Akbar, B. Pinguang-Murphy, *Mater. Des.* **2016**, *94*, 274.
- [87] K. Li, Y. Xie, M. You, L. Huang, X. Zheng, *Biol. Trace Elem. Res.* **2016**, *174*, 198.
- [88] A. Pandey, A. K. Patel, *Nanomaterials* **2018**, *8*, 363.
- [89] B. Moongraksathum, Y.-W. Chen, *Catal. Today* **2018**, *310*, 68.
- [90] Y. A. S. Khadar, A. Balamurugan, V. P. Devarajan, R. Subramanian, *Orient. J. Chem.* **2017**, *33*, 2405.
- [91] M. A. Bonifacio, S. Cometa, M. Dicarolo, F. Baruzzi, S. de Candia, A. Gloria, M. M. Giangregorio, M. Mattioli-Belmonte, E. De Giglio, *Carbohydr. Polym.* **2017**, *166*, 348.
- [92] S. Pourshahrestani, E. Zeimaran, N. Adib Kadri, N. Gargiulo, S. Samuel, S. V. Naveen, T. Kamarul, M. R. Towler, *J. Mater. Chem. B* **2016**, *4*, 71.
- [93] A. Rahimnejad Yazdi, L. Torkan, W. Stone, M. R. Towler, *J. Biomed. Mater. Res. B Appl. Biomater.* **2018**, *106*, 367.
- [94] Q.-M. Zhao, Y.-Y. Sun, C.-S. Wu, J. Yang, G.-F. Bao, Z.-M. Cui, *Nanotoxicology* **2019**, *14*, 289.
- [95] B. R. Barrioni, A. C. Oliveira, M. de Fátima Leite, M. de Magalhães Pereira, *J. Mater. Sci.* **2017**, *52*, 8904.
- [96] Y. Anwar, *Int. J. Biol. Macromol.* **2018**, *111*, 1140.
- [97] J. Vuong, C. Hellmich, *J. Theor. Biol.* **2011**, *287*, 115.
- [98] J. Marchi, *Biocompatible Glasses : From Bone Regeneration to Cancer Treatment, The Evaluation, Control, And Effects of the Compositions of Bioactive Glasses on Their Properties And Applications*, Springer International Publishing, Cham : Imprint: Springer, Cham, **2016**, pp. 85-117.
- [99] S. P. Valappil, D. Ready, E. A. A. Neel, D. M. Pickup, W. Chrzanowski, L. A. O'Dell, R. J. Newport, M. E. Smith, M. Wilson, J. C. Knowles, *Adv. Funct. Mater.* **2008**, *18*, 732.
- [100] A. R. Unnithan, A. Ramachandra Kurup Sasikala, Y. Sathishkumar, Y. S. Lee, C. H. Park, C. S. Kim, *Ceram. Int.* **2014**, *40*, 12003.
- [101] A. Arumugam, C. Karthikeyan, A. S. Haja Hameed, K. Gopinath, S. Gowri, V. Karthika, *Mater. Sci. Eng. C Mater. Biol. Appl.* **2015**, *49*, 408.
- [102] M. Qi, W. Li, X. Zheng, X. Li, Y. Sun, Y. Wang, C. Li, L. Wang, *Front. Mater.* **2020**, *7*, 1.
- [103] T. V. Plakhova, A. Y. Romanchuk, S. N. Yakunin, T. Dumas, S. Demir, S. Wang, S. G. Minasian, D. K. Shuh, T. Tyliczszak, A. A. Shiryaev, A. V. Egorov, V. K. Ivanov, S. N. Kalmykov, *J. Phys. Chem. C* **2016**, *120*, 22615.
- [104] S. Ferraris, M. Cazzola, V. Peretti, B. Stella, S. Spriano, *Front. Bioeng. Biotechnol.* **2018**, *6*.
- [105] E. Yavuz, Ş. Tokaloğlu, H. Şahan, Ş. Patat, *Food Chem.* **2016**, *194*, 463.
- [106] Y. H. Lee, S. Park, K.-G. Lee, M. Y. Lee, K. H. Cho, S. J. Kim, K. T. Nam, *ChemCatChem* **2019**, *11*, 1665.
- [107] F. Corsi, F. Caputo, E. Traversa, L. Ghibelli, *Front. Oncol.* **2018**, *8*, 1.
- [108] B. O. Asimeng, E. K. Tiburu, K. Kan-Dapaah, J. K. Efavi, R. Asiamah, D. W. Afeke, *Cerâmica* **2020**, *66*, 340.
- [109] J. A. Rincón-López, J. A. Hermann-Muñoz, A. L. Giraldo-Betancur, A. De Vizcaya-Ruiz, J. M. Alvarado-Orozco, J. Muñoz-Saldaña, *Materials* **2018**, *11*, 1.
- [110] Z. Zhuang, T. Miki, M. Yumoto, T. Konishi, M. Aizawa, *Procedia Eng.* **2012**, *36*, 121.
- [111] Y. Yu, Z. Bacsik, M. Edén, *Materials* **2018**, *11*, 1.
- [112] C. Drouet, *BioMed Res. Inte.* **2013**, *2013*, 490946.
- [113] H. M. Kim, T. Himeno, M. Kawashita, T. Kokubo, T. Nakamura, *J. R. Soc. Interface* **2004**, *1*, 17.
- [114] J. Weng, Q. Liu, J. Wolke, D. Zhang, K. De Groot, *J. Mater. Sci. Lett.* **1997**, *16*, 335.
- [115] G. Lusvardi, F. Sgarbi Stabellini, R. Salvatori, *Materials* **2019**, *12*, 1.
- [116] M. Franchini, G. Lusvardi, G. Malavasi, L. Menabue, *Mater. Sci. Eng. C Mater. Biol. Appl.* **2012**, *32*, 1401.
- [117] S. Hosseini, H. Farnoush, *Mater. Res. Express* **2018**, *6*, 025404.
- [118] Z. Xu, M. A. Hodgson, P. Cao, *Metals* **2016**, *6*, 309.
- [119] P. Liu, D. Zhang, Y. Dai, J. Lin, Y. Li, C. Wen, *Acta Biomater.* **2020**, *114*, 485.
- [120] E. R. Begley, *Guide to Refractory and Glass Reactions*, Cahners Book Division, Boston, MA **1970**.
- [121] M. R. Filgueiras, G. La Torre, L. L. Hench, *J. Biomed. Mater. Res.* **1993**, *27*, 445.
- [122] S. V. Dorozhkin, *Biomater* **2011**, *1*, 121.
- [123] A. Eriksson, *Bioactivity Testing of Dental Materials*, UPTec Q, Uppsala universitet, Sweden **2019**, pp. 1-35.
- [124] N. Vandecandelaere, C. Rey, C. Drouet, *J. Mater. Sci. Mater. Med.* **2012**, *23*, 2593.
- [125] O. Kaygili, S. Keser, M. Kom, N. Bulut, S. V. Dorozhkin, *Prog. Biomater.* **2016**, *5*, 173.
- [126] T. Tite, A.-C. Popa, L. M. Balescu, I. M. Bogdan, I. Pasuk, J. M. F. Ferreira, G. E. Stan, *Materials* **2018**, *11*, 2081.
- [127] L. T. Bang, B. D. Long, R. Othman, *Sci. World J.* **2014**, *2014*, 969876.
- [128] B. K. Sarma, B. Sarma, *J. Phys.: Conf. Ser.* **2016**, *765*, 012025.
- [129] T. J. Keenan, L. M. Placek, A. Coughlan, G. M. Bowers, M. M. Hall, A. W. Wren, *Carbohydr. Polym.* **2016**, *153*, 482.
- [130] J. Zhang, Q. Zhang, S. Li, Y. Hou, H. Zhang, *Biol. Trace Elem. Res.* **2013**, *151*, 415.
- [131] G. D. Pepa, M. L. Brandi, *Clin. Cases Miner. Bone Metab.* **2016**, *13*, 181.
- [132] H. R. Hirsch, J. Engelberg, *J. Theor. Biol.* **1965**, *9*, 297.
- [133] O. Jung, O. Jung, R. Smeets, R. Smeets, P. Hartjen, P. Hartjen, R. Schnettler, R. Schnettler, F. Feyerabend, M. Klein, N. Wegner, F. Wallther, D. Stangier, A. Henningsen, A. Henningsen, C. Rendenbach, C. Rendenbach, M. Heiland, M. Heiland, M. Barbeck, M. Barbeck, A. Kopp, *Int. J. Mol. Sci.* **2019**, *20*, 255.
- [134] M. J. Stoddart, *Methods and Protocols*, Humana Press, Totowa, NJ Springer, Switzerland **2011**.
- [135] O. Jung, R. Smeets, D. Porchetta, A. Kopp, C. Ptock, U. MIjller, M. Heiland, M. Schwade, B.r. Behr, N. KrΓger, L. Kluwe, H. Hanken, P. Hartjen, *Acta Biomater.* **2015**, *23*, 354.
- [136] E. Grulke, K. Reed, M. Beck, X. Huang, A. Cormack, S. Seal, *Environ. Sci.: Nano* **2014**, *1*, 429.
- [137] A. Wajda, W. H. Goldmann, R. Detsch, A. Grünewald, A. R. Boccaccini, M. Sitarz, *Ceram. Int.* **2018**, *44*, 22698.
- [138] H. J. Kwon, D. Kim, K. Seo, Y. G. Kim, S. I. Han, T. Kang, M. Soh, T. Hyeon, *Angew. Chem., Int. Ed.* **2018**, *57*, 9408.
- [139] E. Alpaslan, H. Yazici, N. H. Golshan, K. S. Ziemer, T. J. Webster, *ACS Biomater. Sci. Eng.* **2015**, *1*, 1096.
- [140] L. Rubio, R. Marcos, A. Hernández, *Chem. Biol. Interact.* **2018**, *291*, 7.
- [141] B. Bouchaud, J. Balmain, G. Bonnet, F. Pedraza, *J. Rare Earths* **2012**, *30*, 559.
- [142] T. Kokubo, H. Takadama, *Biomaterials* **2006**, *27*, 2907.

- [143] J. Clover, M. Gowen, *Bone* **1994**, *15*, 585.
- [144] E. M. Czekanska, M. J. Stoddart, R. G. Richards, J. S. Hayes, *Eur. Cells Mater.* **2012**, *24*, 1.
- [145] M. Lai, C. D. Hermann, A. Cheng, R. Olivares-Navarrete, R. A. Gittens, M. M. Bird, M. Walker, Y. Cai, K. Cai, K. H. Sandhage, Z. Schwartz, B. D. Boyan, *J. Biomed. Mater. Res., Part A* **2015**, *103*, 564.
- [146] S. Staehlke, H. Rebl, B. Nebe, *Cell Biol. Int.* **2019**, *43*, 22.
- [147] J. Lincks, B. D. Boyan, C. R. Blanchard, C. H. Lohmann, Y. Liu, D. L. Cochran, D. D. Dean, Z. Schwartz, *Biomaterials* **1998**, *19*, 2219.